New Very High-Order Upwind Multilayer Compact Schemes with Spectral-Like Resolution for Flow Simulations

Zeyu Bai[1] and Xiaolin Zhong[2]
University of California, Los Angeles, CA, 90095, USA

Hypersonic boundary layer receptivity and stability, transitional and turbulent flows and various other flow problems with complex physics have increased the demand for high-order methods with high resolutions. It is necessary that the high-order methods are robust and accurate in resolving a wide range of time and length scales. This paper presents a new very high-order upwind multilayer compact scheme in the finite difference framework. By introducing first derivatives into the finite difference formulas and approximating the second derivatives, the resolution of the new schemes can be significantly improved. Meanwhile, the proposed scheme maintains the simplicity of finite difference methods and a straight-forward explicit formula is used for good computational efficiency. Fourier analysis and boundary stability analysis show that the new schemes have small dissipation and dispersion in a very wide wave number scales, and stable boundary closure schemes are easily to be derived with the benefits of compact stencil. The accuracies and rates of convergence of the new schemes are validated by numerical experiments of linear wave equation, nonlinear Euler equations and Navier-Stokes equations.

I.Introduction

High-order methods have the advantage of acquiring desired accuracy with fewer grid points in computational domain, which will improve the computational efficiency and facilitate large simulations because of lower demand in computer memory. In the past few decades, direct numerical simulation (DNS) of various flow dynamics problems such as hypersonic boundary layer receptivity, stability, transitional and turbulent flow, and many more, has led to increasing interests in very high-order schemes with high resolutions. For reviews of DNS on these problems, see Refs. [1-3]. A common feature of these flows is the complex physics including a large range of time and length scales in such flow fields which is hard to capture with lower-order schemes. To accurately calculate these flows, the schemes with very High-order accuracy and high resolution for a wide range of wave length scales are essential.

The conventional numerical methods for these problems have been spectral methods, especially for turbulent flow. Spectral methods use combination of basis function like Fourier series or orthogonal polynomials to represent the solution in whole computational domain, which leads to very high resolutions. However, high-order spectral methods have been limited to flows with simple geometries and face difficulties when dealing with complicated boundary conditions. Also, spectral methods have the difficulty in capturing discontinuities such as shock because they assume the solution is smooth.

In an effort to developing high-order methods for complex geometry, some discontinuous high-order methods emerged such as spectral difference methods [4, 5], spectral volume methods [6, 7], spectral element methods [8], discontinuous Galerkin (DG) methods [9-11], etc. These methods use the localized reconstruction within each cell or element and thus are suitable to deal with flow over very complex geometries with unstructured grids. Among the discontinuous methods, DG methods seem to be very promising. They can be very accurate with very high-orders by using the polynomial basis function in each element. Each element only interacts with its neighboring elements which makes it very powerful for parallel computing. However, the implementation of high-order discontinuous methods including DG methods on Navier-Stokes equations is complicated when compared to finite difference or finite volume methods. In addition, multi-dimensional simulation with DG methods is expensive because of the increase of freedoms.

There exist flow problems such as transitional flow, hypersonic boundary layer stability that the geometries can be relatively simple, usually with domain discretized by structured grids, but the flow physics can be complicated.

[1] Graduate student researcher, Mechanical and Aerospace Engineering Department.
[2] Professor, Mechanical and Aerospace Engineering Department, AIAA associate fellow.

The prediction of laminar-turbulent transition over blunt bodies is an example. The shape of the body can be simple and the shock is smooth. However, the transition process is a result of the nonlinear response of laminar boundary layers of forcing disturbances [12, 13], which can originate from many different sources including free stream disturbances, surface roughness and vibrations [14]. Due to the complexity of transient hypersonic flow fields involved in the receptivity process, it is necessary to use high-order numerical methods in the simulation to resolve the wide range of length and time scales of the complex wave fields. Hence, very high-order finite difference schemes have received much attention because of their simple implementation procedures when dealing with structured grids.

Conventional explicit finite difference schemes have difficulty in resolving the wave in very small length scales. As a consequence, the grids need to be very dense to capture those small wave components in transitional and turbulent flows, which will be expensive. In an effort to relax this constraint, spectral-like compact finite difference schemes [15-20] have been developed. The idea is to lower the error at marginal resolution to improve the resolution for high-frequency waves at the expense of allowing more error for low-frequency wave [21]. The maximal truncation order is abandoned on a finite difference stencil to achieve spectral properties which means less dispersive error in large wave number region. Meanwhile, they can still maintain the flexibility to complex boundary condition of finite difference methods.

On the other hand, one of the main difficulties in applying high-order finite difference schemes to practical viscous flow simulations is the numerical instability of boundary closure schemes used on solid wall boundary layer [22]. As a result, in most DNS of transitional and turbulent flows of boundary layer, the orders of accuracy of numerical methods are often limited due to the numerical instability of the boundary closure schemes. Many results have been done to conquer the boundary instability. Zhong [22] proposed a non-uniform grid schemes by using an appropriate grid stretching, and clustering grid points near the boundary to obtain stable high-order boundary closure schemes. Refs. [17, 18] used a prefactorization method to reduce stencil size of compact schemes. By reducing the stencil size, the required number of boundary stencils is also reduced which simplifies the treatment for boundaries.

In this paper, a new upwind multilayer finite difference scheme with very high-order accuracy and compact stencil is developed. The word ‘multilayer’ refers to the idea of not only using value on each node, but also including first derivative in the approximation. Thus, the resolution for short wave length can be increased which shows similar property of spectral methods, and the compact stencil is obtained which benefits the construction of boundary closure schemes. Meanwhile, the standard order can still be maintained so that very high-order accuracy and spectral-like resolution is achieved at the same time, while most spectral-like finite difference schemes reduce it to reach high resolution for shorter length scale. In addition, this method is explicit so the cumbersome matrix inverse operations are avoided. The goal of developing the new methods is to solve flows without shock very accurately, so non-linear schemes are not investigated. The advantage of our new compact scheme is the ability to combine the simplicity of finite difference methods with the spectral properties and very high-order accuracy, so that it’s suitable for the flow with very complex flow physics like transitional and turbulent flows. It should be mentioned that similar ideas have been mentioned in Hermite WENO of Qiu and Shu [23, 24] in the framework of finite volume, where both function value and its first derivative is evolved in time and both is used in the reconstruction, and also they use Hermite WENO as limiters for discontinuous Galerkin methods to solve non-linear problems.

The very high-order upwind multilayer compact scheme is also appropriate for simulations of incompressible flow like computational aeroacoustics. Because the computational aeroacoustics requires very low dissipation and dispersion errors, otherwise the results will be completely degraded [21], our new methods should be suitable for these applications with the spectral-like resolution and low dissipation. For this reason, the present new scheme will be useful for the numerical simulation of complex aerodynamic and aeroacoustic problems for industrial applications.

The paper is organized as follows. In section 2, the derivations of the scheme are illustrated in 1-D and 2-D cases respectively. The Fourier analysis and stability analysis is done to show the accuracy and spectral-like resolution. In section 3, the performance of the scheme on wave equations, Euler equations and compressible Navier-Stokes equations are tested. In section 4, the summary of present work is given and the main progress is concluded.

II.Very High-Order Upwind Multilayer Compact Schemes

In the numerical simulation of flow governed by Navier-Stokes equations, method of lines can be used by separating spatial and temporal discretization. In the spatial discretization, the hyperbolic-type inviscid flux term will cause difficulty on numerical stability. To construct stable numerical algorithm, high-order upwind scheme is commonly utilized to discretize the inviscid flux term. Viscous flux terms can be approximated by high-order central

schemes. This paper derives a family of very high-order upwind multilayer compact schemes for the discretization of convective terms for inviscid flows governed by Euler equations and viscous flows governed by Navier-Stokes equations. A model equation of the inviscid Euler equations is linear wave equation. So, the derivation of the very high-order upwind multilayer compact schemes is illustrated on linear wave equations.

A. One-Dimension Case

The 1-D wave Eq. (1) is used to introduce the scheme for 1-D simulations, where the constant wave speed c >0. Conventional explicit finite difference schemes use only u in the supporting nodes to approximate the first derivative u' (= $\partial u/\partial x$), and result in wide stencil for high-order schemes. For the derivation of the new methods, the gradient of Eq. (1) is taken and the resulting Eq. (2) is called the auxiliary equation,

$$\frac{\partial u}{\partial t} + c\frac{\partial u}{\partial x} = 0, \qquad a \le x \le b \tag{1}$$

$$\frac{\partial (u')}{\partial t} + c\frac{\partial (u')}{\partial x} = 0 \tag{2}$$

where u'' (= $\partial(u')/\partial x$) is the second derivative in space. Instead of approximating the first derivative u' like conventional finite difference scheme, our new schemes treat it as an additional unknown of the linear wave. To solve (u, u'), second derivative u'' needs to be obtained by finite difference approximation from u and u'.

The computational domain for one-dimension wave propagation is a periodic domain of one wave length. It is discretized by uniform grids, with grid spacing h. For a grid points i, the general approximation of the second derivatives is derived from the formula in the form:

$$(u_i)'' = \frac{1}{h^2}\sum_{l=-L_1}^{L_2} a_{i+l}u_{i+l} + \frac{1}{h}\sum_{m=-M_1}^{M_2} b_{i+m}(u_{i+m})' - \frac{\alpha}{(p+2)!}u_i^{(p+2)}h^p \tag{3}$$

where u, u' and u'' are the exact solutions of the function value, first derivative and second derivative on the point. A total of L_1+L_2+1 grid points are used to provide the values needed in the approximation, with L_1 points from the upwind side and L_2 points from the downwind side with respect to the base point i. M_1+M_2+1 points are used to provide first derivatives for the approximation, with M_1 points from upwind side and M_2 points from downwind side. P is the order of the scheme, and α is the coefficient of leading truncation error term. A scheme with this combination of supporting points is termed the L_1-L_2-M_1-M_2 scheme. It's easy to derive the coefficients a_{i+l} and b_{i+m} from Taylor expansion series. The maximum order this approximation can achieve is p_{max} = L_1+L_2+M_1+M_2. When p = p_{max}, the approximation is unique and α is determined by a_l and b_m. When p < p_{max}, α acts as a free parameter and the values of a_{i+l} and b_{i+m} in turn are dependent on α.

The numerical stability of a high-order scheme is critical when applying it to discretize the inviscid flux terms. The idea of deriving a low dissipative upwind scheme is commonly used for both stability and accuracy requirements. The goal in present research is to get a stable high-order upwind scheme for inviscid flux and a central scheme for viscous flux on a same centered stencil. So, the symmetrical centered stencils (L_1=L_2, M_1=M_2) are used and p is set to p_{max} - 1 and p_{max} respectively when deriving the upwind scheme and central scheme. Some schemes on biased stencils will also be analyzed as comparisons to show the low dissipation properties of schemes on centered stencils.

The value and sign of α have very important impacts on the stability of the numerical scheme. Generally, larger α introduces more dissipation and makes scheme more stable. Sign of α determines the upwind or downwind setting of the scheme. These are discussed in later sections.

1-1-1-1 scheme

Using three points stencil for both values and first derivatives as shown in Figure 1, the 1-1-1-1 scheme can be derived. It has the 4th-order accuracy for central scheme and 3rd-order accuracy for upwind scheme. The compactness of the scheme is verified as this order of accuracy is achieved in three points stencil. However, to achieve 3rd-order upwind scheme or 4th-order central scheme, five points stencil is needed in conventional finite difference methods.

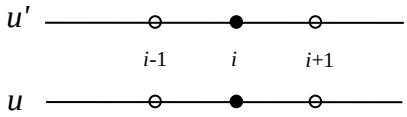

Figure 1. Stencil for 1-1-1-1 scheme for second derivatives

The coefficients of 1-1-1-1 scheme is given in Eq. (4), where α is the free parameter for upwind schemes. α should be set as zero, positive or negative values for central, upwind and downwind schemes. In the Fourier analysis below, recommended value of α for upwind scheme is discussed. Different α values affect the stability, dissipative and dispersive error which determine accuracy. Here, the recommended value 1.5 is given antecedent to the analysis.

$$\begin{aligned} a_{i\pm1} &= 2 \mp \frac{3}{4}\alpha, \qquad a_i = -4, \\ b_{i\pm1} &= \mp\frac{1}{2} + \frac{1}{4}\alpha, \qquad b_i = \alpha. \end{aligned} \tag{4}$$

By choosing some specific α values, the 1-1-1-1 scheme can reduce to upwind schemes on bias stencil. If α = 2, it reduces to 1-1-1-0 scheme, and if α =3/8, it reduces to 1-0-1-1 scheme. Both of them has a large α than the recommend value 1.5. Fourier analysis in later section can show that large α introduces more dissipation, so the upwind schemes on bias stencil are more dissipative than schemes on centered stencil.

2-2-2-2 scheme

Similarly, using five points stencil for both values and first derivatives as shown in Figure 2, the 2-2-2-2 scheme with 8th-order accuracy for central scheme and 7th-order accuracy for upwind scheme can derived. The compactness is significant in 2-2-2-2 scheme compared to conventional finite difference methods, in which nine points need to be used to construct the scheme with same order of accuracy.

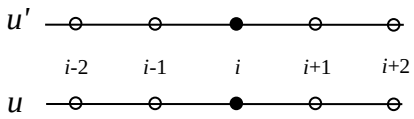

Figure 2. Stencil for 2-2-2-2 scheme for second derivatives

Formulas for 2-2-2-2 scheme are given in Eq. (5). Choosing of α is similar as 1-1-1-1 scheme and recommended value of α is 12 for upwind scheme.

$$\begin{aligned} a_{i\pm2} &= \frac{7}{54} \mp \frac{25}{3456}\alpha, \qquad a_{i\pm1} = \frac{64}{27} \mp \frac{5}{108}\alpha, \qquad a_i = -5, \\ b_{i\pm1} &= \mp\frac{1}{36} + \frac{1}{576}\alpha, \qquad b_{i\pm1} = \mp\frac{8}{9} + \frac{1}{36}\alpha, \qquad b_i = \frac{1}{16}\alpha. \end{aligned} \tag{5}$$

Same as 1-1-1-1 schemes, specific α values generate upwind scheme on bias stencil. If α =16, 2-2-2-1 scheme is obtained, and if α = 17.92, 2-1-2-2 scheme is obtained. Again, both has a large α than the recommended value 12 which corresponds to the low dissipation property of upwind schemes on centered stencil.

Other multilayer compact schemes can be derived following the same idea and formulas are given in Appendix. In general case, stencils for value layer and first derivative layer can be different. It should be mentioned the sign of α for upwind setting on centered stencils are not always the same. For 1-1-1-1 and 2-2-2-2 stencil, positive α generates upwind scheme while negative α works on 2-2-1-1 and 1-1-2-2 stencil.

B. Two-Dimension Case

For multi-dimensional flow simulations, the wave Eq. (6) in multi dimensions is used as the model equation to illustrate the construction of the very high-order upwind multilayer compact scheme. Here, u is a scalar and $\boldsymbol{c} = (c_1, c_2, c_3)$ is a constant velocity vector.

$$\frac{\partial u}{\partial t}+\left(\mathbf{c}\cdot\nabla\right)u=0 \tag{6}$$

For simplicity, we only discuss two-dimensional case and three-dimensional follows the same methodology. In Cartesian grids, it can be written in scalar form as Eq. (7). Then we introduce two auxiliary equations by taking the gradient of Eq. (7). A system of PDEs is consisted of Eqs. (7) - (9), and every equation is solved by method of lines simultaneously.

$$\frac{\partial u}{\partial t}+c_1u_x+c_2u_y=0 \tag{7}$$

$$\frac{\partial\left(u_x\right)}{\partial t}+c_1u_{xx}+c_2u_{xy}=0 \tag{8}$$

$$\frac{\partial\left(u_y\right)}{\partial t}+c_1u_{xy}+c_2u_{yy}=0 \tag{9}$$

The second derivative terms u_{xx}, u_{yy} are approximated the same way as the 1-D case. The cross-derivative terms u_{xy} also need to be approximated from function values and first derivatives, which is not needed in most conventional finite difference methods. It can be derived from Eq. (10). For simplicity, the indexes of the base point i, j is dropped in supporting points and the points with different x and y indexes are numbered uniformly following x-row major order. The truncation term with order p is consists of multiple derivative terms. On a same stencil, the maximum order p_{max} is the same as 1-D case.

$$\left(u_{xy}\right)_{i,j}=\frac{1}{h^2}\sum_l a_lu_l+\frac{1}{h}\sum_m b_m\left(u_x\right)_m+\frac{1}{h}\sum_n c_n\left(u_y\right)_n+o\left(h^p\right) \tag{10}$$

There are much more freedoms in the approximations for cross derivatives because of the choices of corner points in a same stencil from 1-D case. Our goal is to get the simplest formula which includes the least terms and most concise coefficients a_l, b_m, c_n. Upwind setting for cross derivatives can be cumbersome and complicated and only central scheme is used to approximate the cross derivative terms in this paper.

1-1-1-1 scheme

The stencil to approximate the cross derivative u_{xy} for 1-1-1-1 scheme is shown in Figure 3. The base point (i, j) is number as 5. The recommend formula for 1-1-1-1 scheme is given by Eq. (11), where four value points, two x derivative points, and two y derivative points are picked. All the points on the corner are used to provide function values and all the points along a x or y line are used to provide u_x and u_y respectively. No information on the basis point is used and the points are distributed symmetrically, which is similar to the central scheme in 1-D case.

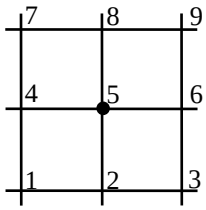

Figure 3. Stencil for 1-1-1-1 scheme for cross derivatives

$$\begin{aligned}\left(u_{xy}\right)_{i,j}=&\frac{1}{h^2}\left(-\frac{1}{4}u_1+\frac{1}{4}u_3+\frac{1}{4}u_7-\frac{1}{4}u_9\right)\\&+\frac{1}{h}\left(-\frac{1}{2}\left(u_x\right)_2+\frac{1}{2}\left(u_x\right)_8\right)+\frac{1}{h}\left(-\frac{1}{2}\left(u_y\right)_4+\frac{1}{2}\left(u_y\right)_6\right)+o\left(h^4\right)\end{aligned} \tag{11}$$

2-2-2-2 scheme

Similarly, the stencil for 2-2-2-2 scheme is shown in Figure 4. The base point (*i*, *j*) is number as 13. The approximation can be constructed by Eq. (12), where sixteen value points, four *x* derivative points, and four *y* derivative points are picked. Similar methodology is followed as in 1-1-1-1 scheme to obtain a simplest form of the formula. All the points which is not on the central *x* and *y* lines are used to provide function values and points on central *x* and *y* lines are used to provide u_x and u_y respectively.

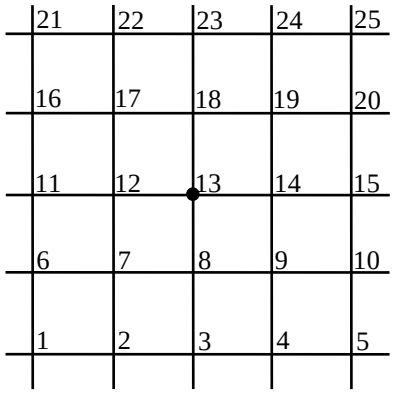

Figure 4. Stencil for 2-2-2-2 scheme for cross derivatives

$$\begin{aligned}\left(u_{xy}\right)_{i,j} = \frac{1}{h^2}&\left(\begin{array}{l}-\frac{1}{144}u_1+\frac{1}{18}u_2-\frac{1}{18}u_4+\frac{1}{144}u_5+\frac{1}{18}u_6-\frac{4}{9}u_7+\frac{4}{9}u_9-\frac{1}{18}u_{10}\\ -\frac{1}{18}u_{16}+\frac{4}{9}u_{17}-\frac{4}{9}u_{19}+\frac{1}{18}u_{20}+\frac{1}{144}u_{21}-\frac{1}{18}u_{22}+\frac{1}{18}u_{24}-\frac{1}{144}u_{25}\end{array}\right)\\ &+\frac{1}{h}\left(\frac{1}{12}\left(u_x\right)_3-\frac{2}{3}\left(u_x\right)_8+\frac{2}{3}\left(u_x\right)_{18}-\frac{1}{12}\left(u_x\right)_{23}\right)+\frac{1}{h}\left(\frac{1}{12}\left(u_y\right)_{11}-\frac{2}{3}\left(u_y\right)_{12}+\frac{2}{3}\left(u_y\right)_{14}-\frac{1}{12}\left(u_y\right)_{15}\right)\\ &+o\left(h^8\right)\end{aligned} \tag{12}$$

Asymmetric stencil can also be used for cross derivatives, however, the derivation will more complicated. Other typical schemes for cross derivatives are given in Appendix.

C. 1-D Fourier Analysis and Numerical Stability

The dissipation and dispersive errors of the multilayer compact schemes can be investigated by Fourier analysis on wave equation. The trial solutions in Fourier mode are of the form:

$$u = \hat{u}e^{\hat{a}t+i\hat{k}x} \tag{13}$$

$$u' = \hat{u}'e^{\hat{a}t+i\hat{k}x} \tag{14}$$

The temporal derivative is assumed to be accurate and doesn't introduce error. Use the compact scheme in Eq. (3) to discretize the spatial derivative *u"*, then the original equation and auxiliary equation become semi-discrete equations as follows,

$$\frac{d}{dt}\left(u_i\right)+cu_i' = 0 \tag{15}$$

$$\frac{d}{dt}\left(u_i'\right)+\frac{c}{h}\left(\frac{1}{h}\sum_{l=-L_1}^{L_2}a_l u_{i+l}+\sum_{m=-M_1}^{M_2}b_m u_{i+m}'\right) = 0 \tag{16}$$

The trial solution in Eq. (13) and (14) can be written in discrete form on uniform grids as follows,

$$u_{i+l} = \hat{u}e^{\hat{a}t+i\hat{k}(x_i+lh)} \tag{17}$$

$$u'_{i+m} = \hat{u}'e^{\hat{a}t+i\hat{k}(x_i+mh)} \tag{18}$$

Plugging Eq. (17) into Eq. (15), the relation between $\hat{u}$ and $\hat{u}'$ can be derived as shown in Eq. (19). Then, plugging Eq. (18) into Eq. (16) and define the non-dimensional amplification factor $a = \frac{\hat{a}h}{c}$, the auxiliary equation can be transformed into a quadratic equation of a as given in Eq.(20),

$$\hat{u}' = -\frac{\hat{a}}{c}\hat{u} \tag{19}$$

$$a^2 + Ba + C = 0 \tag{20}$$

B and C are complex constants which are determined by the coefficients a_l, b_m in finite difference formulas. Equation (20) has two complex solutions which represents the physical mode and spurious mode respectively. The real part of the root a_r is a dissipation factor which is related to stability and dissipative error, and imaginary part a_i is the approximated wave number and it can reveal the dispersive error. For a stable scheme, it is usually required that the real part a_r of all the roots are non-positive. Meanwhile, the deviation of approximate and exact solution will determine the accuracy and the stiffness of the scheme. The exact solution of a as shown in Eq. (21) can be easily derived if spatial derivative is also assumed to be accurate.

$$\begin{aligned} R(a_{exc}) &= 0 \\ I(a_{exc}) &= -\hat{k}h = -k \end{aligned} \tag{21}$$

Figure 5 presents the spectral analysis for the new 7th-order upwind scheme (2-2-2-2) with α = 12, Zhong's 5th-order upwind scheme (3-3-0-0) with α = -6 and Zhong's 6th-order compact scheme (2-2-1-1) with α = 0 and -1 [25]. In Figure 5(a) the dissipation factors are compared. Only physical mode is plotted for the 7th-order scheme. The pure negative dissipation factors show that all these schemes are stable. Zhong's Compact 2-2-1-1 scheme with α = 0 has no dissipation and coincides with the exact solution. With upwind setting, all these schemes show the dissipation in large wave number region. Compared to the explicit scheme, the compact scheme has smaller dissipation when k < 2.4, however, the dissipation grows rapidly and surpass explicit scheme in large wave number region. Both of them have the largest dissipation when $k = \pi$. The new 7th-order upwind scheme is much less dissipative in all the plotted wave number region compared to both compact and explicit upwind scheme. In Figure 5(b) the approximated wave number are plotted as a function of the exact wave number. As we expect, the compact scheme has better resolution than explicit scheme. However, it deteriorates rapidly after k = 2.4 and drops to zero at $k = \pi$, which is the maximum resolution that most explicit and compact finite difference scheme can achieve in theory. The new 7th-order upwind scheme shows high resolving ability for very large wave number which is similar to spectral methods. That means the new compact scheme is much more accurate for very small wave lengths. In other words, it should be able to compute the wave solutions accurately with much less number of grid points. In fact, this advantage is due to the additional information it contains on each grid points, which is the first derivatives. As a result, the maximum resolution can actually reach to $k = 2\pi$. It need to be mentioned that both 7th-order upwind scheme and Zhong's explicit 5th-order upwind scheme use an explicit formula, but the former is constructed on a five-point stencil while the latter need a seven-point stencil. In other words, the resolution of 7th-order scheme is much better on a shorter stencil, which validates the idea that the new scheme can reach very high-order and spectral-like resolution in a very compact stencil.

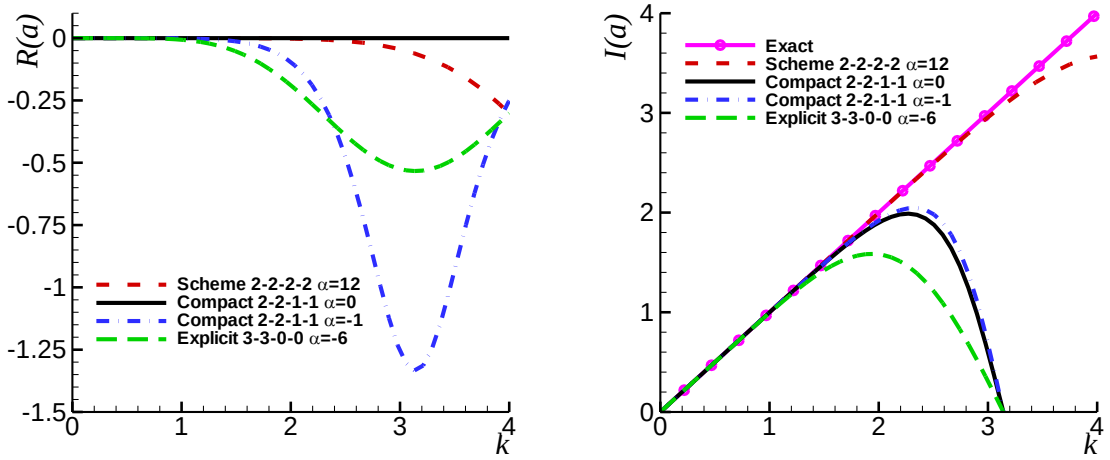

a), Dissipation factor b), Approximate wave number

Figure 5. Fourier analysis results of the new multilayer scheme, Zhong's compact, and explicit schemes[25].

The choice of upwind coefficients has impact on the performance of numerical schemes. In Figure 6, α = 0, 12, 14 are chosen for 2-2-2-2 scheme and comparison with Zhong's 5th-order upwind scheme with α = -6 are given. It is observed that 2-2-2-2 schemes with different upwind coefficients have similar resolution in terms of wave number. All of them are much better than Zhong's 5th-order upwind scheme. In Figure 6(a), the amplification factors of both the physical and spurious modes of 2-2-2-2 scheme are plotted. Different from the physical modes, which are consistent with exact solution for small wave number and deviate in large wave number region, the spurious modes show large damping in small wave number region and this property benefits accuracy because the spurious wave will damp out in the simulation when grid resolution is good enough. Another important information revealed by the dissipation factor of spurious mode is the restriction on the time step size, or termed as stiffness of the scheme. It is well known from the stability analysis theory for ODE that $|\hat{a}\Delta t|$ should fall into the Stability region of time integral scheme. A large amplification factor indicates $|\hat{a}\Delta t|$ will be large for the same time step size, i.e., the integral of the resulting ODE will be more restrictive in terms of choosing time step size if explicit time integral like Runge-Kutta methods are applied. It is shown in Figure 6(a) that larger upwind coefficient will introduce larger damping for spurious modes in small wave number region, which should result in more restrictive time step size. Besides, larger upwind coefficients also make the physical mode more dissipative in large wave number region, which will affect the accuracy when small length wave is important in the flow. For 2-2-2-2 upwind scheme, α = 12 is recommended for stability, dissipation, and stiffness concerns.

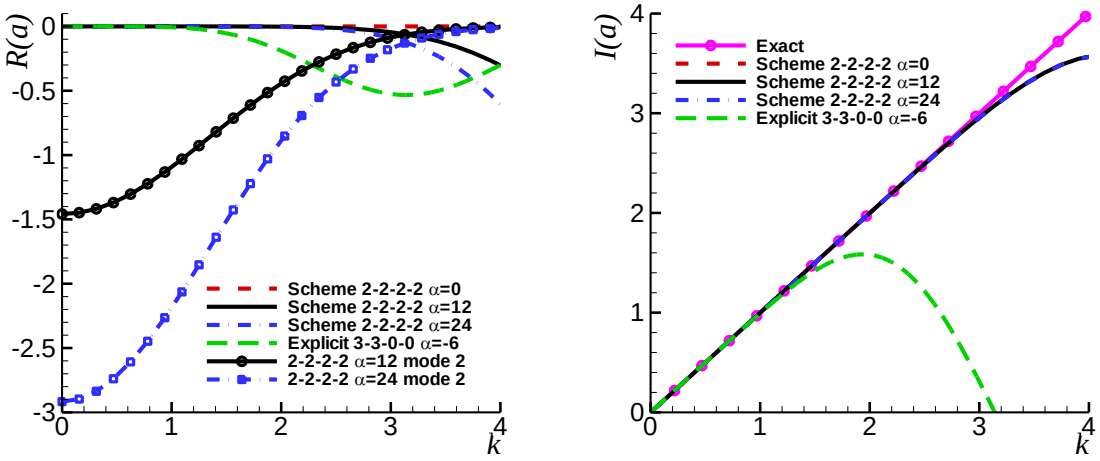

a), Dissipation factor b), Approximate wave number

Figure 6. Fourier analysis results of the 7th-order scheme with different upwind coefficients.

The Fourier analysis results of the 3rd-order scheme on a 1-1-1-1 stencil are presented in Figure 7. As comparison, results of 7th-order 2-2-2-2 upwind scheme and Zhong's 5th-order upwind scheme are also shown. It is observed that 1-1-1-1 scheme has larger dissipation factor compared to 2-2-2-2 scheme, as well as error in approximate wave number. It indicates that high-order multilayer scheme is more accurate than low-order scheme in terms of both dissipative and dispersive error. However, when the 1-1-1-1 scheme is compared with Zhong's 5th-order explicit scheme, it is noticed that the new 3rd-order scheme shows much better resolving ability for large wave number than Zhong's 5th-order upwind scheme even with lower order and a much narrower stencil of three gird points. This advantage can be explained by the additional information contained on each grid points. Figure 7(a) shows that the new 3rd-order scheme has less dissipation than Zhong's 5th-order scheme in most wave number region, which means the 1-1-1-1 scheme are less dissipative. Increasing upwind coefficients introduces more dissipation for both modes, same as 2-2-2-2 scheme, and it also decrease the resolving ability slightly as observed in Figure 7(b). Considering stability, dissipation, and stiffness, the recommended value for α is 1.5 for 1-1-1-1 scheme.

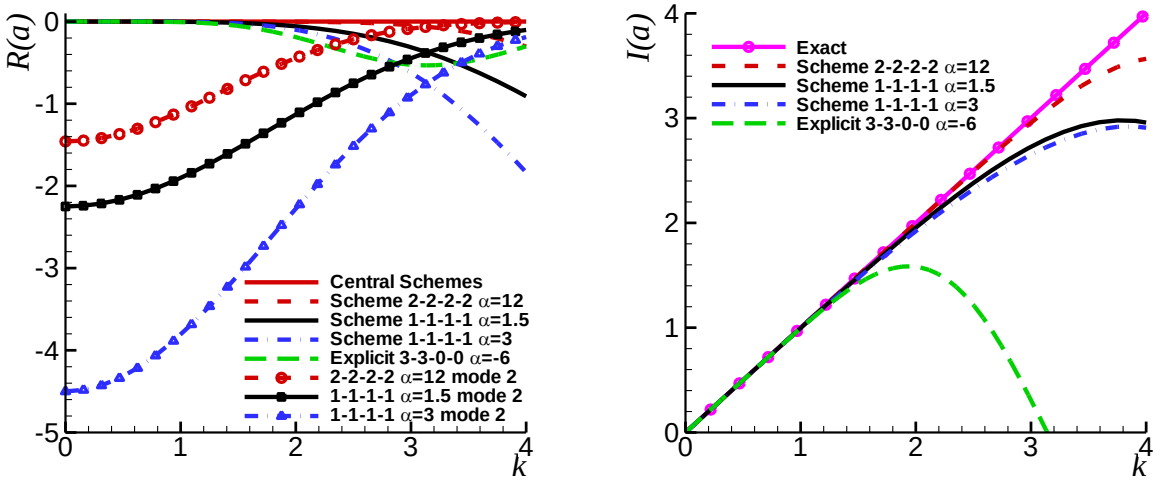

a), Dissipation factor

b), Approximate wave number

Figure 7. Fourier analysis results of the 3rd-order scheme with different upwind coefficients.

The traditional upwind schemes usually use upwind-bias stencil. It has enough numerical dissipation to control the aliasing errors and is very stable[25]. Instead, the presented upwind scheme and Zhong's compact and explicit upwind scheme[25] use centered stencil and adjustable coefficient in the leading dissipative truncation term. To compare these two different type stencils, the Fourier analysis results of the 5th-order (2-1-2-1) and 6th-order (2-1-1-1, 1-1-2-1) upwind compact schemes on bias stencils and above 7th-order upwind compact scheme (2-2-2-2) on centered stencil are presented in Figure 8. It is observed that all the schemes have spectral-like resolution and 2-1-2-1 scheme which uses upwind-bias stencil for both value and derivative grid points shows the smallest error in approximate wave number. However, plots of dissipation factor show that 2-1-2-1 has largest dissipation. As a comparison, 2-2-2-2 scheme on a centered stencil has smallest dissipation but the resolution is slightly lower than 2-1-2-1 scheme in large wave number region. This observation is consistent with the conclusion in [25] that upwind scheme on centered grid stencil have smaller dissipation than upwind-bias grid stencil. 2-1-1-1 and 1-1-2-1 schemes which mix center and bias stencil have similar property but the latter is slightly more dispersive and less dissipative. It can be concluded that using bias stencil on value points introduces more dissipation than same setting on derivative points. Figure 8(c) plots spurious mode and physical mode together for the three upwind schemes on bias stencils. It indicates that using bias stencil will also introduce larger dissipation on spurious modes which will cause more restrictive time step size. So, it is more appropriate to use upwind setting on centered stencils in the construction of the upwind multilayer compact schemes to make them more stable but less dissipative.

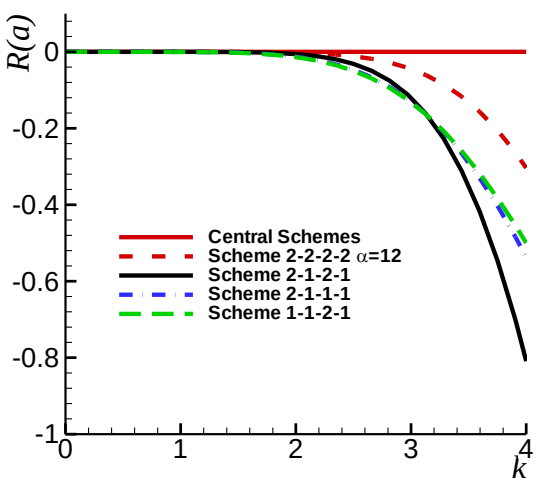

a), Dissipation factor

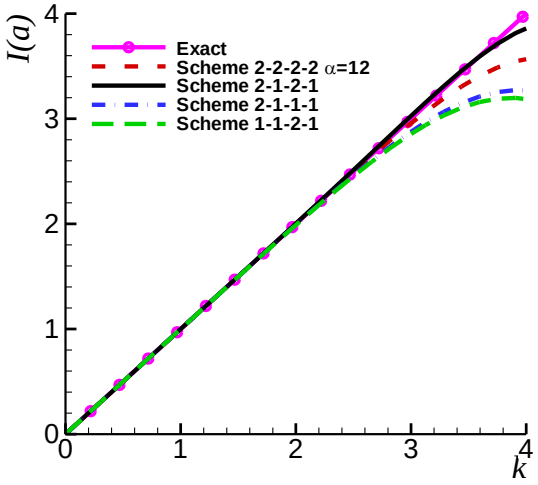

b), Approximate wave number

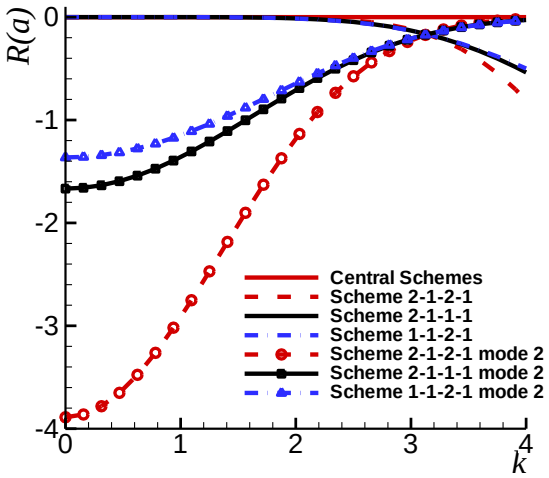

c), Physical modes and spurious modes

Figure 8. Comparison of upwind schemes on centered stencil and bias stencil.

Pure upwind setting which is based on a fully bias stencil can also be used to construct the upwind multilayer scheme as in the construction of conventional upwind scheme. However, they may not be stable. 2-0-2-0 scheme uses value and first derivative only from upwind side to approximate second derivative and the dissipation factor and approximate wave number are compared with 2-2-2-2 upwind scheme and Zhong's explicit upwind scheme (3-3-0-0) in Figure 9. Figure 9(a) shows 2-0-2-0 scheme has a positive real part in a which means the error will be amplified during simulations. The approximate wave number of 2-0-2-0 scheme deviates the exact solution in a different manner as 2-2-2-2 scheme and Zhong's explicit upwind scheme as observed in Figure 9(b). Because of the using of first derivatives, the effect of fully bias stencil on numerical stability is more complicated and need further investigation. But it can be speculated that too much imbalance on the stencil may cause instability. It is more appropriate to construct upwind multilayer scheme on centered stencils or semi-bias stencils.

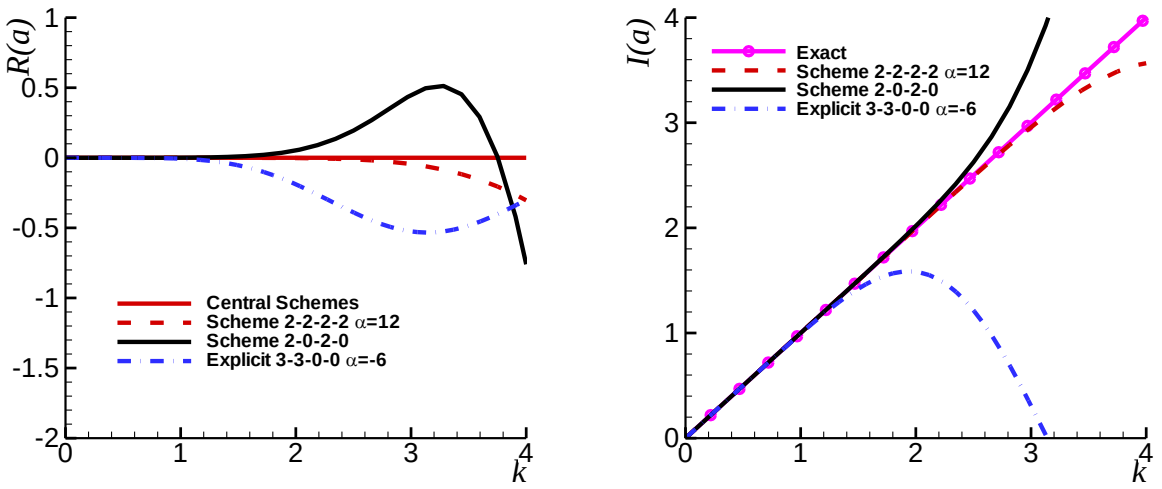

a), Dissipation factor b), Approximate wave number

Figure 9. Fourier analysis results of the upwind scheme on a one-side bias stencil.

D. 2-D Fourier Analysis and Numerical Stability

For multi-dimensional simulations, the approximation of the cross derivatives terms given in Eq. (10) is needed. Cross derivative approximation may also have impact on the stability and dissipative properties of the numerical scheme. The Fourier analysis above can be extended in two-dimensional domain. Because the discretization is based on Cartesian coordinates, the wave propagation angle θ and Fourier wave angle φ should be taken into consideration. The wave equation and two auxiliary equations are already given in Eqs. (7), (8), and (9), where $c_1 = c\cdot\cos\theta$ and $c_2 = c\cdot\sin\theta$. Fourier trial solutions are of the form in Eqs. (22), (23), (24).

$$u = \hat{u}e^{\hat{a}t+i\hat{k}(x\cos\varphi+y\sin\varphi)} \tag{22}$$

$$u_x = \hat{u}_x e^{\hat{a}t+i\hat{k}(x\cos\varphi+y\sin\varphi)} \tag{23}$$

$$u_y = \hat{u}_y e^{\hat{a}t+i\hat{k}(x\cos\varphi+y\sin\varphi)} \tag{24}$$

The procedure of the 2-D Fourier analysis follows the same methodology as in 1-D analysis. Plugging the trial solution into Eq. (7), a relation between $\hat{u}$, $\hat{u}_x$ and $\hat{u}_y$ can be derived as shown in Eq. (25). Plugging the formulas of second and cross derivatives into Eqs. (8) and (9), a cubic equation of a in the form of Eq. (26) can be derived. Same as 1-D analysis, A, B, and C are complex constants determined by the finite difference formulas, but they are also dependent on θ and φ in 2-D analysis. Three roots of the equation correspond to one physical mode and two spurious modes. The real and imaginary part of a plays the same role as in 1-D analysis.

$$\hat{u} = -\frac{c}{\hat{a}}\left(\hat{u}_x\cos\theta + \hat{u}_y\sin\theta\right) \tag{25}$$

$$a^3 + Aa^2 + Ba + C = 0 \tag{26}$$

The exact solution of a is given in Eq.(27). The real part is same as 1-D analysis and the imaginary part is the product of 1-D solution and a cosine function of θ and φ.

$$\begin{aligned} R(a_{exc}) &= 0 \\ I(a_{exc}) &= -k\cos(\theta-\varphi) \end{aligned} \tag{27}$$

In the 2-D Fourier analysis and 2-D numerical simulations in this paper, the upwind scheme with recommended α value is used for second derivatives and the corresponding central scheme is applied to cross derivatives. The

overall accuracy depends on the second derivatives terms when there is no boundary closure considered. Different wave propagation angles and phase angles for trial solutions are considered in the Cartesian coordinates. Because of the interchangeability of x and y axis, the cases with angles from 45° to 90° are repetition of (0°, 45°) region. For simplicity, only results of 0° and 45° are presented, one represents the situation with zero angles and the other represents non-zero angles cases.

Firstly, the 2-D Fourier analysis of 3rd-order 1-1-1-1 scheme are considered. Figure 10(a) plots the dissipation factors for a propagating wave in x-axis direction (θ = 0°), and Figure 10(b) shows results for a propagating wave in $x = y$ direction (θ = 45°). Three different modes are observed in all the results, mode 1 is the physical mode and mode 2 and 3 are two spurious modes. In 1-D Fourier analysis, only mode 1 and 2 exist and these two modes in 2-D analysis behavior similarly as one-dimensional analysis. When both θ and φ are 0, the results reduce to 1-D Fourier results in Figure 7. The dissipation factor of mode 3 depends on both θ and φ. When θ is zero, it's always zero which means mode 3 will keep its initial condition during the simulation. When θ is not zero but φ is zero, the dissipation factor of mode 3 is a negative constant which means the mode 3 will be evenly decayed for all the wave components. When both θ and φ is not zero, mode 3 behaviors similarly like mode 2. Beside the additional spurious mode, there is a slightly positive part in $R(a)$ of physical modes when both θ and φ are not zero. Figure 10(b) show the details of the positive dissipation factor. For 1-1-1-1 scheme, the peak locates at k = 1.8 and the magnitude is about 2.5×10^{-3}. However, there is no instability observed in the 2-D flow simulation with 1-1-1-1 scheme presented in this paper.

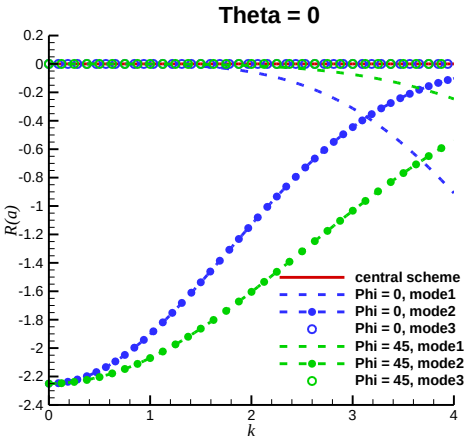

a), Wave propagation in x-axis direction

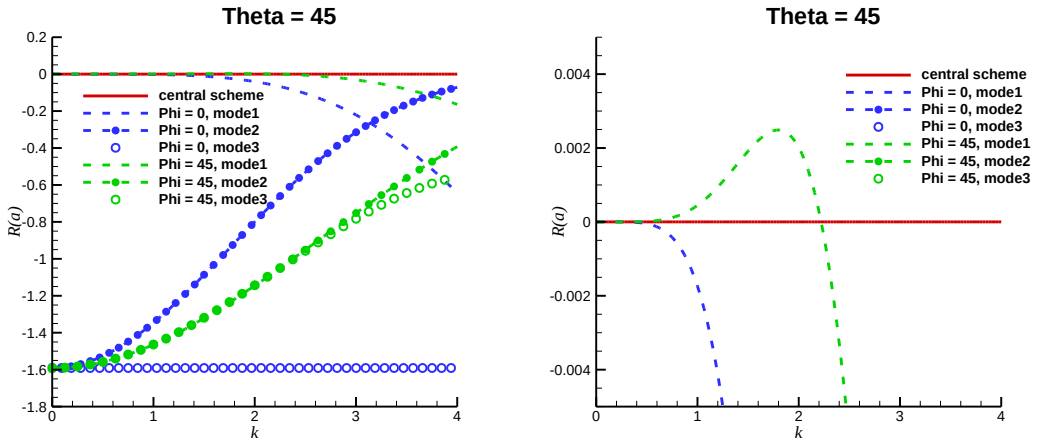

b), Wave propagation in $x = y$ direction

Figure 10. Dissipation factor of 1-1-1-1 scheme for 2-D wave propagation.

The approximate wave number for 1-1-1-1 scheme is shown in Figure 11. All the results with different angles show good resolution in small wave number region, however, the resolution decreases when there is a non-zero angle in θ or φ. This property of finite difference scheme is well known as anisotropy error for multi-dimensional

simulations. The angle between wave propagation and the coordinate (θ) has dominated impact on the resolution. When θ is zero, the scheme has better resolving ability while that in non-zero θ situation is obviously reduced.

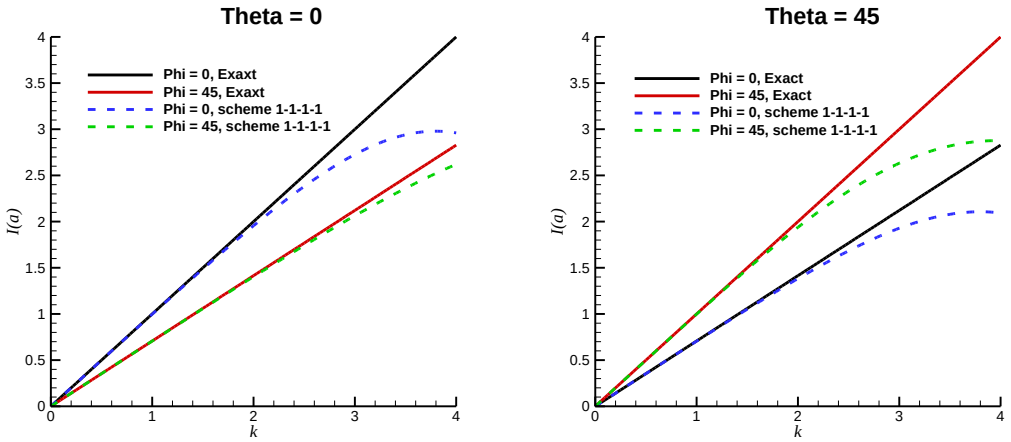

a), Wave propagation in x-axis direction b), Wave propagation in $x = y$ direction

Figure 11. Approximate wave number of 1-1-1-1 scheme for 2-D wave propagation.

2-D Fourier analysis for 2-2-2-2 scheme is presented in Figure 12. Same as 1-D Fourier analysis, all modes in 2-2-2-2 scheme are less dissipative than those of 1-1-1-1 scheme, indicating that the 2-2-2-2 scheme is more accurate. There is also a positive part in the dissipation factor of the physical mode. Compared to the 1-1-1-1 scheme, the peak appears when k = 3.0 which moves towards high wave number region and the magnitude is increased to 4.0×10^{-3}. This may indicate 2-2-2-2 scheme are more unstable than 1-1-1-1 scheme in 2-D simulation. However, there is still no instability observed in the 2-D flow simulation with 2-2-2-2 scheme.

The inconsistency between Fourier analysis and numerical results is probably due to nonlinearity of the governing equations (Euler or Navier-Stokes equations), or the dissipation introduced in the temporal integration like Runge-Kutta methods. On the other hand, the magnitude of the positive part in $R(a)$ is so small with a magnitude of 10^{-3}, as a comparison the peak in Figure 9 is 0.5, it may be easily overwhelmed by any other dissipation in numerical simulations. Because there is so many degrees of freedom in the approximation of cross derivatives, it is also possible that there exists a better choice of the formulas for cross derivatives which can produce stable dissipation factor in Fourier analysis. But compared to second derivatives, the effects of cross derivative terms on stability is not the main concern of the proposed numerical scheme from our experience in simulation.

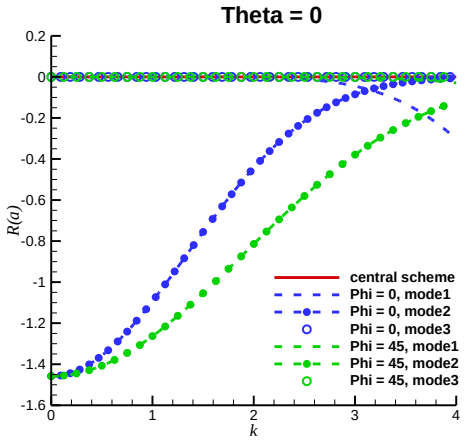

a), Wave propagation in x-axis direction

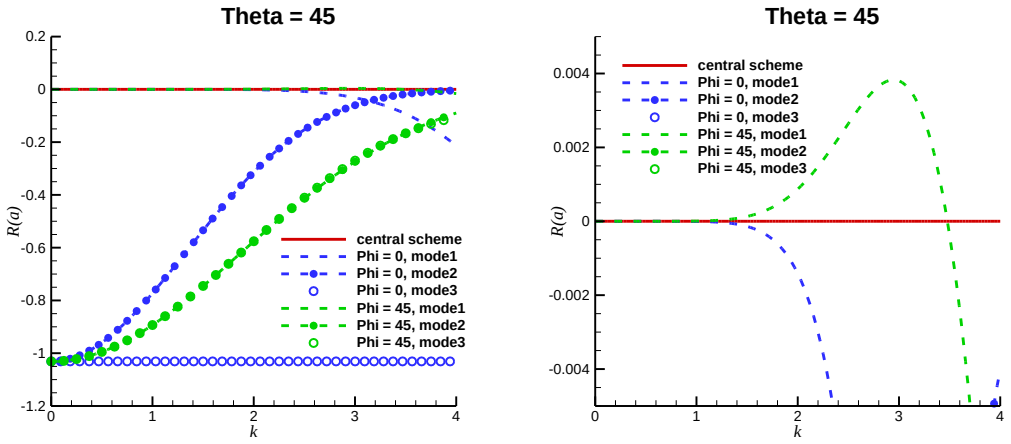

b), Wave propagation in $x = y$ direction

Figure 12. Dissipation factor of 2-2-2-2 scheme for 2-D wave propagation.

The approximate wave number for 2-2-2-2 scheme is shown in Figure 13. Comparing to 1-1-1-1 scheme, same effects of θ and φ on the resolving ability can be observed but the resolution in large wave number region is significantly increased for all cases. So, 2-2-2-2 scheme is more accurate than 1-1-1-1 scheme in 2-D simulations as well.

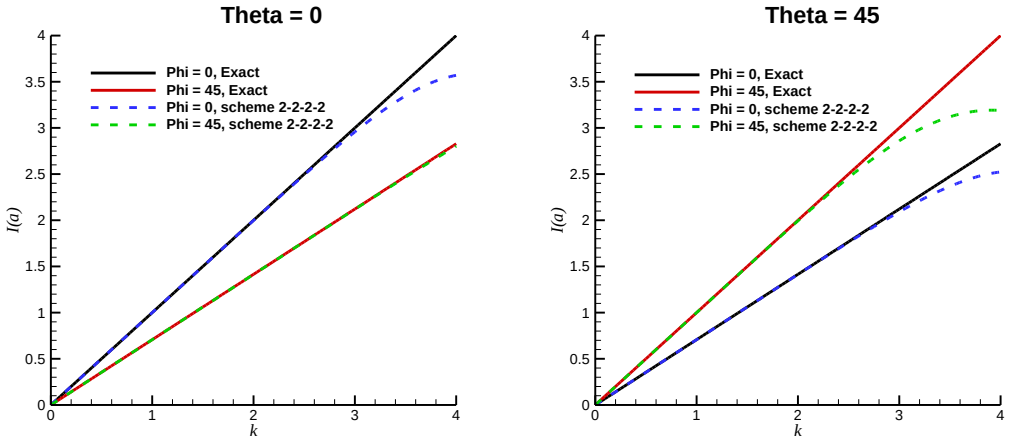

a), Wave propagation in x-axis direction b), Wave propagation in $x = y$ direction

Figure 13. Approximate wave number of 2-2-2-2 scheme for 2-D wave propagation.

E. Comparison with Discontinuous-Galerkin (DG) Methods

Recently, Discontinuous-Galerkin (DG) methods have attracted more attentions because of their high accuracy and flexibility to complex geometry surrounded by unstructured mesh. In this section, the proposed multilayer compact scheme is compared with DG methods of Cockburn & Shu [11] by Fourier analysis. All other versions of DG methods will behavior similarly. For simplicity, a more straightforward derivation of DG methods on uniform structured mesh is given in this paper. More general formulas can be find in paper [11].

Standard Legendre polynomials of order l are represented with respect to x in the form of Eq. (28), where x is the local coordinate with range of [-1, 1]. $C_j^{(l)}$ are coefficients only dependent on l. Eq. (28) can also be generalized in matrix and vector form in Eq. (29), where $\mathbf{P}(x) = (P^{(0)}(x), P^{(1)}(x),\ldots, P^{(n)}(x))^T$, $\mathbf{x} = (1, x,\ldots, x^{(n)})^T$, $\mathbf{A}$ is the lower triangular matrix containing $C_j^{(l)}$ constants, the elements up to $n = 5$ are given in Eq. (30). The dimension for $\mathbf{P}(x)$, $\mathbf{x}$ and $\mathbf{A}$ is $(n+1)$, $(n+1)$, $(n+1)\times(n+1)$ respectively.

$$P^{(l)}(x) = C_0^{(l)} + C_1^{(l)} x + \ldots + C_l^{(l)} x^l = \sum_{j=0}^{l} C_j^{(l)} x^j \tag{28}$$

$$\mathbf{P}(x) = \mathbf{A} \cdot \mathbf{x} \tag{29}$$

$$\mathbf{A} = \begin{bmatrix} 1 & 0 & 0 & 0 & 0 & 0 \\ 0 & 1 & 0 & 0 & 0 & 0 \\ -\frac{1}{2} & 0 & \frac{3}{2} & 0 & 0 & 0 \\ 0 & -\frac{3}{2} & 0 & \frac{5}{2} & 0 & 0 \\ \frac{3}{8} & 0 & -\frac{30}{8} & 0 & \frac{35}{8} & 0 \\ 0 & \frac{15}{8} & 0 & -\frac{70}{8} & 0 & \frac{63}{8} \end{bmatrix} \tag{30}$$

In a computational cell *i*, Legendre polynomials can be used as basis function to represent the dependent variable u_i as shown in Eq. (31), where *n* is highest degree of Legendre polynomials, $u_i^{(l)}$ are the weight of the Legendre polynomial of order *l*. u_i can also be represented in matrix form, where $\mathbf{u}_i(t) = (u_i^{(0)}(t), u_i^{(1)}(t),\ldots, u_i^{(n)}(t))$. Thus, $\mathbf{u}_i(t)$ is the only unknown for cell *i* which has *n*+1 degrees of freedom. It should be noticed that in the *N*th-order DG methods, *N* = *n*+1, so the number of unknowns in each cell equals to the order of accuracy. If *N* = 1, the only unknown is $u_i^{(0)}(x)$ and DG methods recovers to 1st-order finite volume methods.

$$u_i(x,t) = \sum_{l=0}^{n} u_i^{(l)}(t) P^{(l)}(x) = \mathbf{u}_i(t) \cdot \mathbf{P}(x) \tag{31}$$

Same as multilayer schemes, the discretization of DG methods is demonstrated using the wave equation. Weak form of the wave equation for numerical simulation is derived by multiplying Legendre polynomials $P^{(l)}(x)$ with different orders to Eq. (1) and integrate *x* from [-1,1] in each cell, as shown in Eq. (33). Plugging Eq. (31) into Eq. (33), then integrating the convection term by part and applying the orthogonality of Legendre polynomials in Eq. (32), the weak form equation can be derived, which is given in Eq. (34). It need to be noticed that $u_i(1, t)$, $u_i(-1, t)$ are the boundary function values, which are discontinuous in neighboring cells in DG methods. Different ways to determine boundary values will lead to different DG methods.

$$\int_{-1}^{1} P^{(l)}(\xi) P^{(m)}(\xi) d\xi = \begin{cases} \dfrac{2}{2l+1} = \gamma^{(l)}, & m = l \\ 0, & m \neq l \end{cases} \tag{32}$$

$$\frac{d}{dt} \int_{-1}^{1} P^{(l)}(\xi) u_i(\xi,t)\, d\xi + c \int_{-1}^{1} P^{(l)}(\xi) \frac{\partial}{\partial \xi} \left[u_i(\xi,t) \right] d\xi = 0 \tag{33}$$

$$\gamma^{(l)} \cdot \frac{d}{dt} u_i^{(l)}(t) + c \left[P^{(l)}(1) u_i(1,t) - P^{(l)}(-1) u_i(-1,t) \right] - c \int_{-1}^{1} u_i(\xi,t) \frac{d}{d\xi} \left(P^{(l)}(\xi) \right) d\xi = 0 \tag{34}$$

Using matrix form, the derivative of Legendre polynomials in the last term of Eq. (34) can be easily represented by itself as shown in Eq. (35), where **C** is a constant matrix.

$$\frac{d}{dx} \mathbf{P}(x) = \mathbf{C} \cdot \mathbf{P}(x) \tag{35}$$

Combining Eqs. (31), (34), (35) and applying orthogonality of Legendre polynomials again, an ODE system for cell *i* in Eq. (36) can be derived. Again, both **E** and **D** is constant matrix which can be acquired easily.

$$\mathbf{E} \frac{d}{dt} \mathbf{u}_i(t) + c \left[\mathbf{P}(1) u_i(1,t) - \mathbf{P}(-1) u_i(-1,t) - \mathbf{D} \cdot \mathbf{u}_i(t) \right] = 0 \tag{36}$$

Finally, simple upwind idea is applied to the boundary value $u_i(1, t)$, $u_i(-1, t)$, i.e., all the boundary values are determined from the left cell. Then,

$$u_i(1,t) = \mathbf{u}_i(t) \cdot \mathbf{P}(1)$$
$$u_i(-1,t) = u_{i-1}(1,t) = \mathbf{u}_{i-1}(t) \cdot \mathbf{P}(1) \tag{37}$$

Plugging Eq. (37) into Eq. (36), a system of semi-discrete equations as shown in Eq. (38) is derived. The form is very similar to finite difference methods but containing the weight matrix **H** and **K**. After figuring out **H** and **K**, it's straightforward to perform Fourier analysis on DG methods. Also, it's easy to conduct numerical simulation using Eq. (38) directly if evenly distributed grid points are used. To make it general for other mesh setting, a coordinate transformation is needed to convert the equations to physical domain. It will not be discussed in this paper and more details can be referred to Cockburn & Shu's methods [11].

$$\frac{d}{dt}\mathbf{u}_i(t) = c\left[\mathbf{H} \cdot \mathbf{u}_i(t) - \mathbf{K} \cdot \mathbf{u}_{i-1}(t)\right] \tag{38}$$

Fourier analysis on DG methods is very similar to multilayer compact schemes. The difference is that for DG methods with 3rd-order or higher accuracy, there are more degrees of freedom than our multilayer schemes. So, it's more general to use matrix form for the trial Fourier solution as shown in Eq. (39). Discrete form on uniform mesh is in Eq. (40) where h is the grid spacing. Plugging Eq. (40) into Eq. (38) and following the same methodology as in section II(C) and II(D), the approximate value of $a = \frac{\hat{a}h}{c}$ can be solved.

$$\mathbf{u}(x,t) = \hat{\mathbf{u}} e^{\left(\hat{a}t + i\hat{k}x\right)} \tag{39}$$

$$\mathbf{u}_i(t) = \hat{\mathbf{u}} e^{\left(\hat{a}t + i\hat{k}x_i\right)}, \quad \mathbf{u}_{i-1}(t) = \hat{\mathbf{u}} e^{\left(\hat{a}t + i\hat{k}(x_i - h)\right)} \tag{40}$$

The *N*th-order DG methods (DG-*N*) has *N* degrees of freedom which leads to *N* complex roots of *a*. As a result, there are a total of *N* Fourier modes including one physical mode and *N*-1 spurious modes.

The Fourier analysis results of 2nd-order DG methods (DG-2) are shown in Figure 14. Same as our multilayer schemes, DG-2 have two degrees of freedom in each cell. One physical and one spurious mode are observed. For all DG methods, the dissipation factor of physical mode always start from 0 and spurious modes always have negative dissipation factor in small wave number region, which is consistent with our multilayer schemes. In Figure 14(a), both modes have non-positive dissipation factors in the whole wave number region, which means DG-2 is stable. However, the damping is very large. In Figure 14(b), the approximate wave number for physical mode overlaps on the exact solution (solid line) in a very wide wave number region, indicating that the resolving ability for large wave number region is very good even though the scheme is only second order.

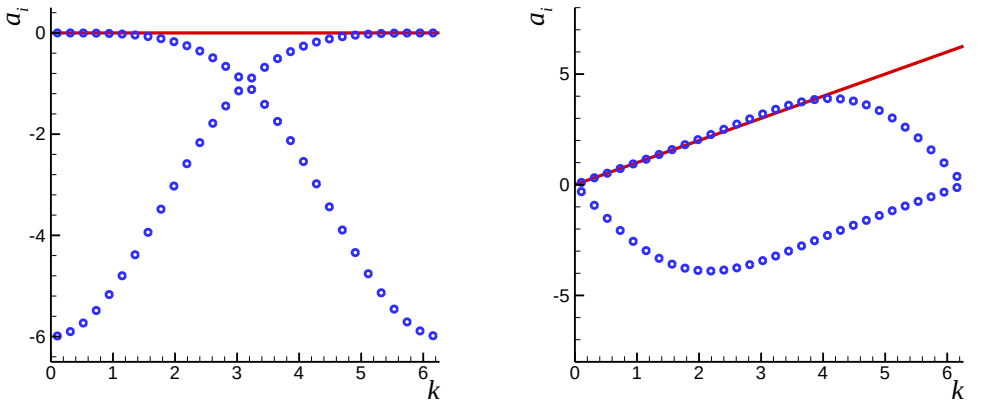

a), Dissipation factor b), Approximate wave number

Figure 14. Fourier analysis results of the DG-2 scheme.

Figure 15 shows the results of 3rd-order DG methods (DG-3), different from DG-2 and our multilayer scheme. A second spurious mode is observed and it's very dissipative with a minimum value of -12 in dissipation factor. As comparison, the lowest point for 1-1-1-1 scheme with α = 1.5 is -2.2 and that for 2-2-2-2 scheme with α = 12 is -1.5.

It is mentioned in the analysis above that the largest magnitude of $R(a)$ has impact on the time step size. Thus, according to Fourier results, DG-3 should have much more restrictive stability condition on Δt compared to our multilayer compact scheme. The good side of DG-3 is that it's still stable for the linear wave. Moreover, the approximate wave number in Figure 15(b) shows a very good resolution for large wave number region. Even in the region near $k = 2\pi$ which is the upper boundary for DG-2 and our multilayer scheme, DG-3 still has good performance. Compared to our 2-2-2-2 scheme in Figure 6 and 1-1-1-1 scheme in Figure 7, DG-3 shows better resolutions on high frequency waves, which more closely resemble spectral solution.

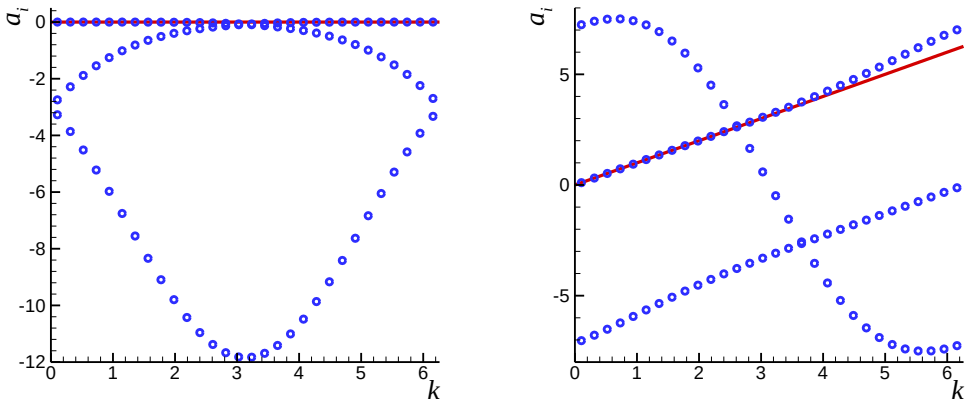

a), Dissipation factor b), Approximate wave number

Figure 15. Fourier analysis results of the DG-3 scheme.

The improvement of resolution in large wave number region is due to increase of information in each cell. Equation (41) gives a relation between the upper boundary of wave number (k_{max}) a numerical scheme can approximate and the degrees of freedom (K) in each cell.

$$k_{max} = K\pi \tag{41}$$

K equals to 1 for conventional finite difference and finite volume methods; K equals to 2 for our multilayer compact scheme; and K equals to N for an Nth-order DG methods. So, high-order DG methods have the advantage of resolving very small wave length in the flow.

Comparison of different order DG methods is given in Figure 16. DG-1 is same as 1st-order finite volume or finite difference methods and only one physical mode exists in the result. With the increase of order, both dissipative and dispersive error is significantly decreased. Figure 16(b) shows clearly that the upper boundary of approximate wave number for an Nth-order DG methods is $k = N\pi$.

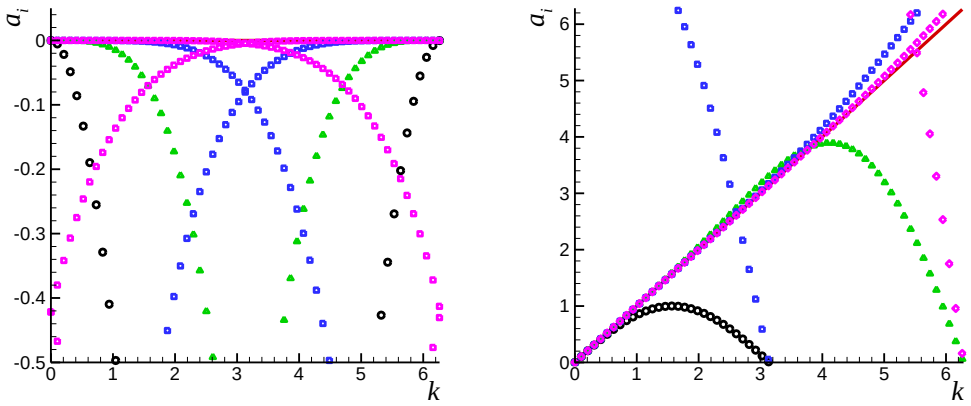

a), Dissipation factor b), Approximate wave number

Figure 16. Comparison of DG methods from 1st to 4th-order.

(black: DG-1, green: DG-2, blue: DG-3, Purple: DG-4)

More Fourier analysis results of higher order DG methods indicate that DG methods are always stable for linear wave whatever the expected order is. Increasing the order will also improve the resolving ability especially for high frequency wave. This is reasonable because the maximum wave number a numerical scheme can approximate is mainly dependent on the degrees of freedom on each grid point or cell. However, higher orders will introduce more spurious modes and the large dissipation factors in these modes will restrict the stability condition for time integral. To give a strong demonstration on both advantage and disadvantage of DG methods, Figure 17 shows the Fourier results of 6th-order DG methods (DG-6). It is clear that the approximate wave number of physical mode perfectly overlap with exact solution in the range of [0, 2π], indicating the high resolution for linear waves in very small scales. Meanwhile, the lowest point in dissipation factor is about -38, which is about 25 times of the value in our 7th-order 2-2-2-2 scheme. Although all modes are stable, time step size must be very small to meet stability condition.

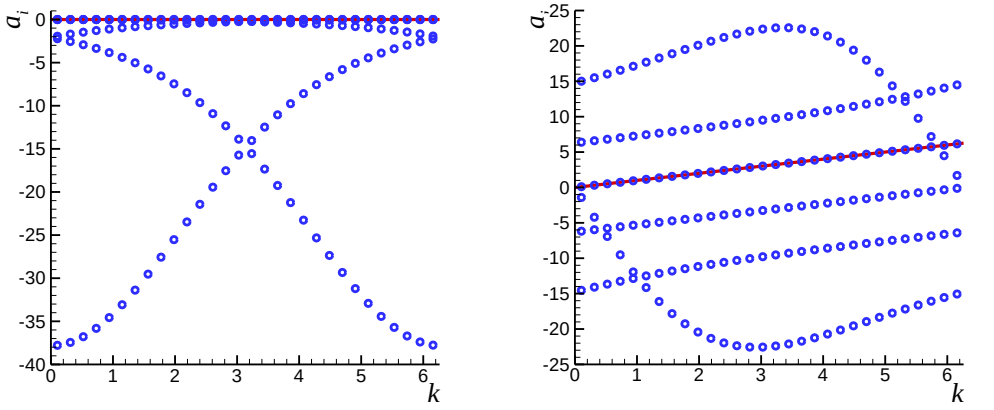

a), Dissipation factor b), Approximate wave number

Figure 17. Fourier analysis results of the DG-6 scheme.

In summary, Fourier analysis on DG methods above and analysis on our new schemes in section II(C) indicate that, 1) the proposed multilayer compact schemes have larger error than high-order DG methods ($N > 3$) for extremely small length waves ($k > \pi$), but show comparable resolution for waves in moderate length scales ($k < \pi$); 2) our new schemes have much more relaxed stability condition for time integral. Other obvious advantage of our methods to DG methods is the simplicity and computational efficiency on structured mesh, which is commonly used for simple geometries. With the increase of accuracy, DG methods need more memory requirement due to more degrees of freedom. The limitation of memory is even more obvious for multi-dimensional simulation. If the flow simulation requires very high accuracy and the geometry is simple, such as hypersonic boundary layer simulation over blunt body[25], the multilayer compact scheme is more appropriate than DG methods.

F. Stability of Boundary Closure Schemes

High-order finite difference methods often require boundary closure schemes at grid points on or near the boundaries of the computational domain. When the inner scheme is coupled with boundary closure schemes, the stability can be affected. It's widely known that for a *p*th order inter schemes, the stable boundary closure scheme can be (*p*-1)st order to maintain the global accuracy of inner scheme. Matrix method is an easy way to analyze the stability of boundary closure schemes. Implementation details for conventional finite difference methods can be found in Ref. [25]. In this paper, the extension to the multilayer compact scheme is illustrated. Same as Fourier analysis, the boundary stability is also implemented on 1-D wave equation and its auxiliary equation as shown in Eq. (1) and (2).

Two boundaries are set on a finite domain, the left boundary is assumed to be an inlet with known boundary conditions and right boundary is solved from wave equation. N+1 uniform gird points are used to discretize the domain, the left boundary is located at $i = 0$ and the right boundary is located at $i = N$. The two partial differential equations can be transformed into a system of ODEs by using the above compact scheme for the inner points and boundary closure schemes for the boundary points. The resulting equations can be combined and represented in a matrix form as Eq. (42),

$$\frac{d}{dt}\begin{bmatrix}\mathbf{U}\\ \mathbf{U}'\end{bmatrix}+c\begin{bmatrix}\mathbf{0} & \mathbf{I}\\ \mathbf{A} & \mathbf{B}\end{bmatrix}\cdot\begin{bmatrix}\mathbf{U}\\ \mathbf{U}'\end{bmatrix}=\begin{bmatrix}\mathbf{0}\\ \mathbf{g}(t)\end{bmatrix} \tag{42}$$

where $\mathbf{U} = (u_1, \ldots, u_N)^T$, $\mathbf{U}' = (u'_1, \ldots, u'_N)^T$, $\mathbf{g}(t)$ are a matrix containing u_0 - the non-periodic boundary condition given at $x = 0$. **A** and **B** are matrices which consist of the coefficients of both inner schemes and boundary closure schemes. The coupled boundary closure schemes are also multilayer compact schemes but on bias stencil. All the formulations can be found in the Appendix. $c = 1$ is used in the analysis and the equations can be written into standard form,

$$\frac{d}{dt}\overline{\mathbf{U}} = \mathbf{M}\cdot\overline{\mathbf{U}} + \mathbf{G}(t) \tag{43}$$

where **M** only depends on the formulas of inner and boundary closure schemes.

$$\overline{\mathbf{U}} = \left(\mathbf{U}, \mathbf{U}'\right)^T, \quad \mathbf{M} = -\begin{bmatrix}\mathbf{0} & \mathbf{I}\\ \mathbf{A} & \mathbf{B}\end{bmatrix} \tag{44}$$

Usually the boundary source terms $\mathbf{G}(t)$ can be ignored in stability analysis. The asymptotic stability condition for the semi-discrete equations is that all eigenvalues of the matrix **M** contain no positive real parts.

Firstly, the boundary stability of 3rd-order inner scheme (1-1-1-1) is analyzed. 1-1-1-1 scheme uses three-point stencil and only the two ends need to be dealt with by boundary closure schemes. Figure 18 shows the eigenvalue spectrum when 2nd-order boundary closure schemes are used on both ends, i.e., 0-1-0-1 scheme for the left end and 1-0-1-0 scheme for the right end. α is the upwind coefficients for inner scheme which can stabilize the high-order boundary closures. The eigenvalues show that larger α causes the spectrum move towards negative direction, which means the scheme is more stable. An unexpected result is that even with central scheme ($\alpha = 0$) on inner points, 2nd-order boundary closure schemes are still stable though the eigenvalues have real parts that are very close to 0. The central scheme is usually considered unstable because it contains no numerical dissipation. However, the boundary closure scheme on a bias stencil (2-0-2-0) near the right end might have stabilization effect as upwind schemes that can introduce enough damping into the system. As a result, the central scheme becomes stable.

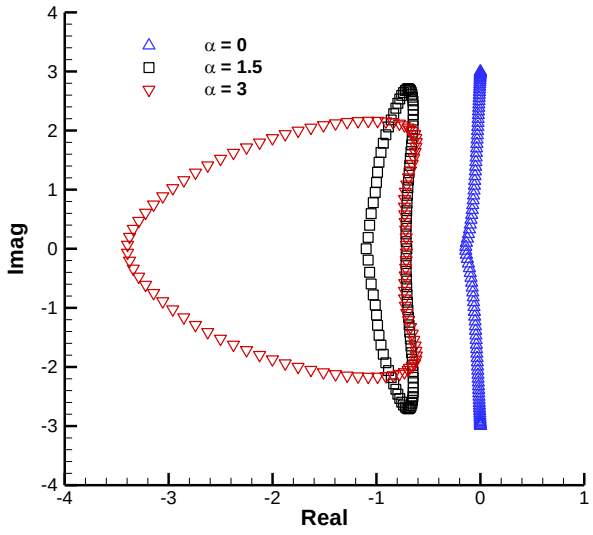

Figure 18. Eigenvalue spectrum for the 3rd-order upwind scheme (1-1-1-1) with 2nd-order boundary closure schemes (0-1-0-1, 1-0-1-0).

Figure 19 shows the eigenvalue spectrum when 3rd-order boundary closure schemes are coupled with 1-1-1-1 scheme. It turns out the eigenvalue spectrum is very similar to Figure 18. No positive real part of eigenvalues is observed for all α choices. It can be concluded from Figure 18 and Figure 19 that both 2nd and 3rd-order boundary

closure schemes are stable when coupled with 1-1-1-1 scheme. 1-1-1-1 scheme is very stable in terms of boundary stability. The use of upwinding in inner schemes helps to stabilize boundary closure schemes. The value for α is still chosen to be 1.5 to keep enough dissipation and maintain accuracy at the same time.

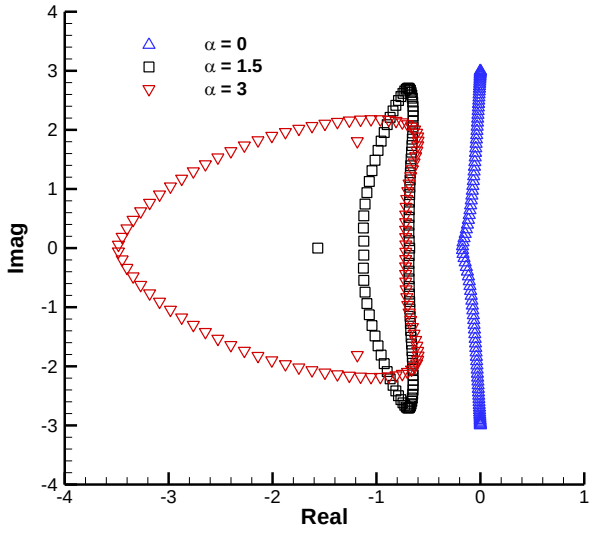

Figure 19. Eigenvalue spectrum for the 3rd-order upwind scheme (1-1-1-1) with 3rd-order boundary closure schemes (0-2-0-1, 2-0-1-0).

Then, the boundary stability of 7th-order inner scheme (2-2-2-2) is analyzed. 2-2-2-2 scheme uses five-point stencil and four boundary closure schemes are needed, two for the end points and two for the boundary adjacent points. Multilayer compact schemes with various orders on bias stencil can be coupled with the 2-2-2-2 inner scheme. Figure 20 shows the eigenvalue spectrum when 6th-order boundary closure schemes are used on both ends and their adjacent points. Different from 1-1-1-1 inner scheme, the 2-2-2-2 inner scheme with $\alpha = 0$ is not stable which generates positive real parts in the eigenvalue spectrum. Again, increasing α can stabilize the boundary closure schemes. When $\alpha = 12$, which is the recommended value from Fourier analysis above, the 6th-order boundary closure schemes are stable. When α has a value of 24 the dissipation is already very large. So, $\alpha = 12$ is still the recommended choice for the simulation with boundaries.

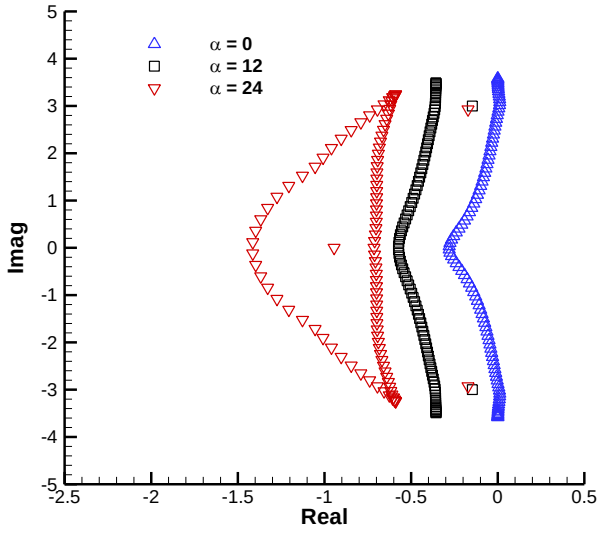

Figure 20. Eigenvalue spectrum for the 7th-order upwind scheme (2-2-2-2) with 6th-order schemes on end points (0-3-0-3, 3-0-3-0) and 6th-order schemes on adjacent points of boundaries (1-2-1-2, 2-1-2-1).

Stability of 7th-order boundary closure schemes is also analyzed with 2-2-2-2 inner scheme. Figure 21 shows the eigenvalue spectrum with same 7th-order inner scheme and 6th-order boundary schemes on the end points, but 7th-order schemes on the boundary adjacent points. Compared to Figure 20, the continue spectrum distribution doesn't change obviously, but the positions of discrete eigenvalue points move towards positive direction significantly, which indicates the increase of order of boundary closure schemes causes instability on 2-2-2-2 inner scheme. In Figure 21, the two discrete eigenvalues represented by the black squares have positive real parts, indicating that the inner scheme with α value of 12 doesn't have enough dissipation to stabilize the system when coupled with 7th-order schemes on the boundary-adjacent points. If α is increased to 24, the boundary closure schemes become stable again, however, the dissipation on inner points will be too large. Similar results are observed if 7th-order boundary closure schemes are used on end points and the boundary adjacent points, as shown in Figure 22.

From the matrix analysis above, it is recommended to use 6th-order boundary closure schemes on both ends and their adjacent points when 2-2-2-2 scheme is used on inner points. The value for α is chosen to be 12 to provide enough dissipation to stabilize the boundary closure schemes.

Comparing the results of 2-2-2-2 and 1-1-1-1 schemes, we find that the high-order multilayer compact schemes has more severe boundary instability problem than low-order schemes, which is a common feature of all finite difference schemes. But due to the compactness of stencil, there are only four boundary closures schemes required even for the 7th-order scheme. This advantage over conventional finite difference schemes is obvious. As a comparison, Zhong's 5th-order explicit scheme needs six boundary closure schemes for flow simulations with boundaries.

It should be mentioned that in the matrix $\mathbf{G}(t)$ in Eq. (43), the value of first derivative u' on the inlet is needed due to the multilayer formulation of our new scheme. However, u' usually depends on the neighboring points and should be approximated. There are various ways to approximate u' and they may affect the stability of boundary closure schemes as well. Discussion on this problem is not finished and will be left for future research.

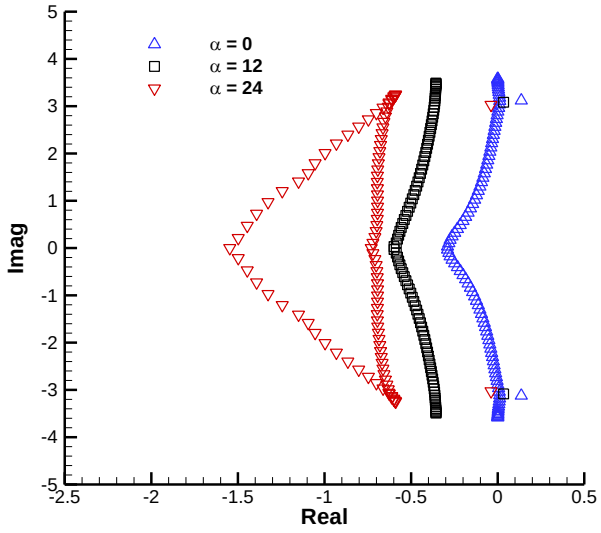

Figure 21. Eigenvalue spectrum for the 7th-order upwind scheme (2-2-2-2) with 6th-order schemes on end points (0-3-0-3, 3-0-3-0) and 7th-order schemes on adjacent points of boundaries (1-3-1-2, 3-1-2-1).

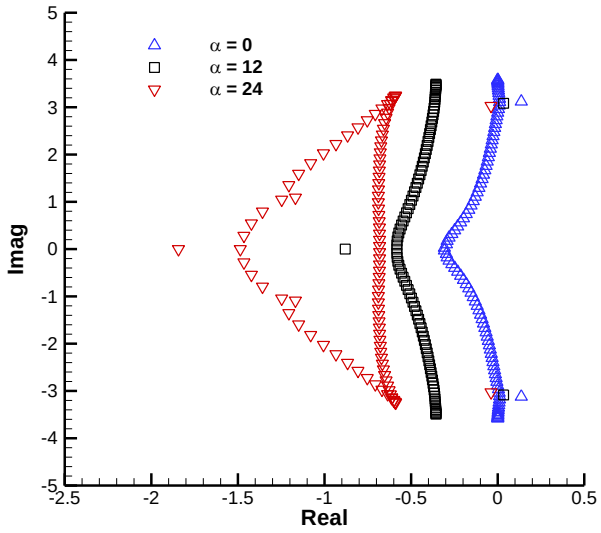

Figure 22. Eigenvalue spectrum for the 7th-order upwind scheme (2-2-2-2) with 7th-order schemes on end points (0-4-0-3, 4-0-3-0) and 7th-order schemes on adjacent points of boundaries (1-3-1-2, 3-1-2-1).

In chapter II, the new very high-order upwind multilayer compact scheme are illustrated on the linear wave equations. By Fourier analysis and stability analysis, the spectral-like resolution of the new scheme can be validated. Compared to Zhong's 5th-order upwind scheme, both the new 7th-order and 3rd-order schemes have much better resolution on the large wave number region. Besides, the stencils are more compact because more degrees of freedom on each grid points. Compared to high-order DG methods, which have extremely high resolutions on linear waves, our new schemes have less restrictive stability condition and better computational efficiency. Due to the compactness of stencil, stable boundary closure schemes are also easy to obtain.

III.Numerical Results

The new very high-order upwind multilayer compact schemes are tested and validated in the linear wave equation, nonlinear Euler equations, and compressible Navier-Stokes equations in this chapter. Several test cases in 1-D and 2-D computational domain are used. The numerical solutions are compared with analytical solutions and the accuracy is evaluated by grid refinement. The schemes are firstly applied to the computations of linear waves. Zhong's 5th-order upwind scheme, DG methods are also used as comparisons. Then, the performances on nonlinear Euler equations are validated through the simulation of convective flow, acoustic wave, and isentropic vortex. In the Navier-Stokes simulation, the new schemes are applied to two-dimensional steady Couette flow. The perfect-gas assumption is used in compressible Navier-Stokes equations. The focus of the numerical tests is on the high-order accuracy and high resolution property when number of grid points is restricted. Because our new scheme is designed for the simulation of smooth flow fields without discontinuity, there is no test case of shock-capturing simulations for Euler equations or Navier-Stokes equations.

A. Linear Wave Equation

The new very high-order upwind multilayer compact scheme is firstly tested on linear 1-D wave equation as shown in Eq. (1) and (2). Periodic boundary conditions are set on both sides of the domain. The parameters of the calculations are $a = 0$, $b = 1$, $c = 1$. $N + 1$ uniform grid points are used. A sinusoidal wave is resolved by the new scheme. The initial condition (t=0) and exact solution is given as Eq. (45).

$$u(x,t) = 2\sin\left[6\pi(x-ct)+0.5\right] \qquad c = 1 \tag{45}$$

The comparison between Zhong's 5th-order upwind scheme with α = -6 [25] and new 7th-order (2-2-2-2) upwind scheme with α = 12 is given. Both calculations use 4th-order Runge-Kutta scheme for time marching. It

need to be mentioned that larger CFL number can be used to satisfy stability condition, but in order to compare spatial discretization errors, CFL number is set to 0.005 to reduce error from the time integral.

The results at t = 1 when N = 7, 9, 15 are shown in Figure 23. The curve is the exact solution for the wave propagation, the squares and triangles are solution of new 7th-order scheme and Zhong's 5th-order scheme respectively. As expected, when N = 15, the error for Zhong's 5th-order scheme is large and 7th-order scheme can resolve the wave very well. As the mesh reduces to N = 7 and 9, the new scheme is still able to resolve the wave accurately while the old scheme completely loses the resolving ability. This indicates the new compact scheme has good resolution for components with very small wave lengths and even very coarse grids (N = 7) can achieve the same level of resolution as fine grids (N = 15) in conventional finite difference scheme.

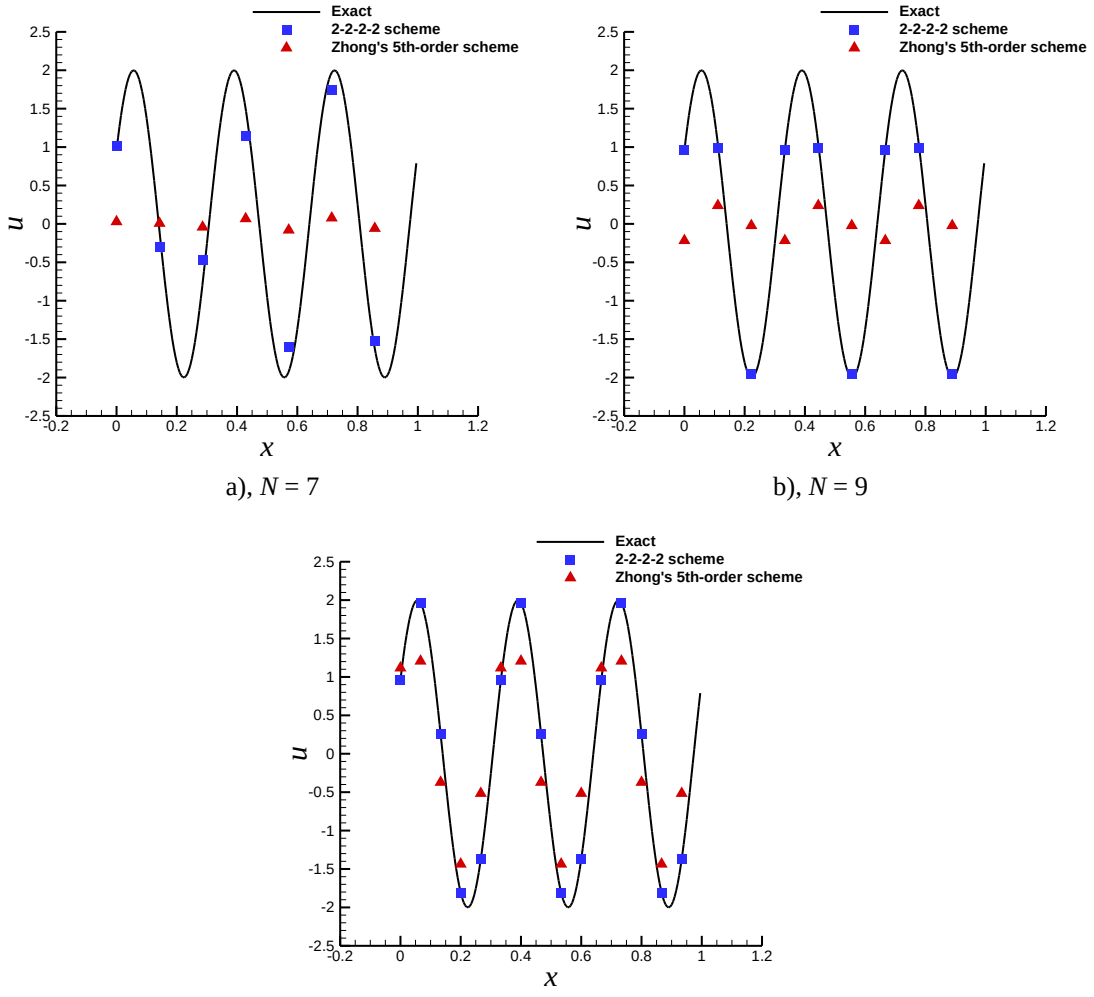

a), N = 7

b), N = 9

c), N = 15

Figure 23. Computational results for the one-dimensional linear wave equation with periodic boundary conditions.

To analyze the performance of numerical schemes quantitively, errors between numerical and analytical results are checked, and grid refinement is performed to estimate rate of convergence. Table 1, Table 2, Table 3 give the errors and rates of convergence of 1-1-1-1 scheme, 2-2-1-1 scheme and 2-2-2-2 scheme with recommended α, which leads to 3rd, 5th, 7th-order upwind scheme respectively. As N increases, the numerical error reduces significantly. When N increases to 10, the magnitude of errors of 1-1-1-1 scheme is already one order smaller than the wave amplitude which is 2 and relative error is less than 45%. In 2-2-1-1 and 2-2-2-2 schemes, it's two orders smaller than the wave amplitude and relative error is less than 5% and 1.5% respectively. This quantitive analysis of errors validates the good resolution of our new scheme with a small number of grid points. The grid refinement results show that the expected order is reached for all three schemes. In Table 1 and Table 3, when N is larger than 80, the estimated order is even higher than the expected order, which indicates the upwind scheme is very accurate in the simulation of linear waves.

Table 1. Errors and rates of convergence of 3rd-order (1-1-1-1) upwind scheme for wave equation.

N	1-1-1-1 scheme, α = 1.5					
	L1 error	Order	L2 error	Order	L∞ error	Order
5	1.40E+00	\	1.57E+00	\	2.16E+00	\
10	5.62E-01	1.31	6.42E-01	1.29	8.69E-01	1.31
20	6.76E-02	3.06	7.56E-02	3.09	1.07E-01	3.02
40	5.65E-03	3.58	6.28E-03	3.59	8.88E-03	3.59
80	3.93E-04	3.85	4.37E-04	3.85	6.17E-04	3.85
160	2.54E-05	3.95	2.82E-05	3.95	3.98E-05	3.95

Table 2. Errors and rates of convergence of 5th-order (2-2-1-1) upwind scheme for wave equation.

N	2-2-1-1 scheme, α = -1					
	L1 error	Order	L2 error	Order	L∞ error	Order
5	2.16E+00	\	2.36E+00	\	3.33E+00	\
10	6.76E-02	5.00	7.75E-02	4.93	1.05E-01	5.00
20	1.44E-03	5.56	1.59E-03	5.60	2.25E-03	5.54
40	3.53E-05	5.35	3.92E-05	5.34	5.54E-05	5.34
80	9.36E-07	5.24	1.04E-06	5.24	1.47E-06	5.24
160	2.22E-08	5.40	2.47E-08	5.40	3.49E-08	5.40

Table 3. Errors and rates of convergence of 7th-order (2-2-2-2) upwind scheme for wave equation.

N	2-2-2-2 scheme, α = 12					
	L1 error	Order	L2 error	Order	L∞ error	Order
5	1.33E+00		1.47E+00		2.05E+00	
10	1.87E-02	6.15	2.09E-02	6.13	2.89E-02	6.15
20	1.32E-04	7.15	1.46E-04	7.16	2.06E-04	7.13
40	8.39E-07	7.29	9.32E-07	7.29	1.32E-06	7.29
80	4.39E-09	7.58	4.88E-09	7.58	6.90E-09	7.58
160	1.93E-11	7.83	2.14E-11	7.83	3.03E-11	7.83

As a good comparison for our multilayer compact scheme, DG methods are also used to calculate the wave equation. The procedure is already illustrated in chapter II section E. Table 4 shows the errors and rates of convergence of DG-2, which has the same degrees of freedom as our new scheme. It can be observed that the 2nd-order accuracy is achieved except on first two mesh group. Although the resolution is similar to our multilayer compact scheme according to the Fourier analysis, the error of DG-2 are much larger than 1-1-1-1, 2-2-1-1 or 2-2-2-2 scheme due to the larger dissipation of DG-2. However, when mesh is very coarse with only 5 grid points, DG-2 has comparable accuracy with our multilayer schemes, showing the high resolution for wave modes with very small length in Fourier analysis (Figure 14).

Table 4. Errors and rates of convergence of DG-2 scheme for wave equation.

N	DG-2					
	L1 error	Order	L2 error	Order	L∞ error	Order
5	1.29E+00	\	1.43E+00	\	1.99E+00	\
10	1.01E+00	0.35	1.16E+00	0.30	1.56E+00	0.35
20	2.75E-01	1.88	3.05E-01	1.93	4.30E-01	1.86
40	4.50E-02	2.61	5.01E-02	2.61	7.08E-02	2.60
80	7.25E-03	2.63	8.06E-03	2.64	1.14E-02	2.64
160	1.28E-03	2.50	1.42E-03	2.50	2.01E-03	2.50

The numerical simulation results of 3rd and 5th-order DG methods are presented in Table 5 and Table 6. With the increase of the order, errors of DG methods decrease significantly on all meshes. Comparing DG methods to the same order multilayer schemes, i.e. DG-3 vs 1-1-1-1 scheme and DG-5 vs 2-2-1-1 scheme, we find that DG methods have smaller error on all mesh settings. Accompany with the increase of order, the advantage of DG methods' resolving ability becomes more significant. The difference of error magnitude between DG-3 and 1-1-1-1 scheme is one order, while it is two orders between DG-5 and 2-2-1-1 scheme. However, this improvement of resolution is due to increase of freedoms which requires larger memory. On the other hand, although high-order DG methods are more accurate than same order multilayer scheme for linear waves, our new scheme has the advantage of simplicity and computational efficiency of finite difference methods, while higher order DG methods will be complicated in implementation, and very expensive and restrictive in time step.

Table 5. Errors and rates of convergence of DG-3 scheme for wave equation.

N	DG-3					
	L1 error	Order	L2 error	Order	L∞ error	Order
5	9.06E-01	\	1.01E+00	\	1.40E+00	\
10	7.42E-02	3.61	8.15E-02	3.64	1.15E-01	3.61
20	4.92E-03	3.91	5.48E-03	3.90	7.74E-03	3.89
40	5.55E-04	3.15	6.17E-04	3.15	8.71E-04	3.15
80	6.93E-05	3.00	7.69E-05	3.00	1.09E-04	3.00
160	8.67E-06	3.00	9.63E-06	3.00	1.36E-05	3.00

Table 6. Errors and rates of convergence of DG-5 scheme for wave equation.

N	DG-5					
	L1 error	Order	L2 error	Order	L∞ error	Order
5	1.31E-02	\	1.45E-02	\	2.02E-02	\
10	3.69E-04	5.15	4.10E-04	5.15	5.69E-04	5.15
20	1.12E-05	5.04	1.25E-05	5.04	1.76E-05	5.01
40	3.59E-07	4.96	3.99E-07	4.97	5.62E-07	4.97
80	1.15E-08	4.97	1.28E-08	4.96	1.80E-08	4.96
160	3.59E-10	5.00	3.98E-10	5.00	5.63E-10	5.00

B. Euler Equations

Euler equations are the governing equations for inviscid flows. Equation (46) is the Euler equations in conservative form. U is the conservative variables and F_j are the inviscid fluxes. E_t is the total energy per unit volume for perfect gas.

$$\frac{\partial U}{\partial t}+\frac{\partial F_j}{\partial x_j}=0 \tag{46}$$

$$U=\left[\rho,\rho u_1,\rho u_2,\rho u_3,E_t\right] \tag{47}$$

$$F_j=\begin{bmatrix}\rho u_j\\ \rho u_1u_j+p\delta_{1j}\\ \rho u_2u_j+p\delta_{2j}\\ \rho u_3u_j+p\delta_{3j}\\ \left(E_t+p\right)u_j\end{bmatrix} \tag{48}$$

$$E_t=\frac{p}{\gamma-1}+\frac{1}{2}\rho u_ku_k \tag{49}$$

In 2-D calculation, Eqs. (50) and (51) is the auxiliary equations derived for the new scheme. Second and cross derivative terms of inviscid flux F_j are approximated by Eqs. (3) and (10) respectively. The analytical expression of $(F_j)_x$, $(F_j)_y$ are needed in the schemes and they can be derived by taking derivative of Eq. (48). $(F_j)_x$, $(F_j)_y$ are functions of U, U_x, U_y, which are already known before each step in temporal integral.

$$\frac{\partial U_x}{\partial t}+\frac{\partial\left(F_j\right)_x}{\partial x_j}=0 \tag{50}$$

$$\frac{\partial U_y}{\partial t}+\frac{\partial\left(F_j\right)_y}{\partial x_j}=0 \tag{51}$$

The new upwind schemes are applied to the system of Eqs. (46), (50), (51) by flux splitting methods or by applying the schemes in each characteristic field. A locally global Lax-Friedrichs approach to split the inviscid flux F_j and their first derivatives $(F_j)_x$, $(F_j)_y$ is proposed in this paper. Both the inviscid flux and their derivatives are split into positive and negative wave fields as shown in Eq. (52). The positive and negative parts are approximated independently using upwind and downwind schemes.

$$\begin{aligned}
&F_j=F_j^+ + F_j^-\\
&\left(F_j\right)_{x_k}=\left(F_j\right)^+_{x_k}+\left(F_j\right)^-_{x_k}\\
&\left(F_j\right)_{x_k x_j}=\left(F_j\right)^+_{x_k x_j}+\left(F_j\right)^-_{x_k x_j}
\end{aligned} \tag{52}$$

It is required that the flux F_j^+ and F_j^- contains only positive and negative eigenvalues respectively. The approach in Eq. (53) can be used to construct F_j^+ and F_j^-,

$$\begin{aligned}
F_j^+&=\frac{1}{2}(F_j+\Lambda U)\\
F_j^-&=\frac{1}{2}(F_j-\Lambda U)
\end{aligned} \tag{53}$$

where, Λ is a positive parameter which is large enough to make F_j^+ and F_j^- contain only positive and negative eigenvalues. Besides, Λ needs to be constant for the splitting of first derivatives of flux in Eq. (54). It's reasonable to use set a constant Λ in the whole domain, however, the dissipation will be too large especially for low order methods like 1-1-1-1 scheme.

$$\begin{aligned}
\left(F_j\right)^+_{x_k}&=\frac{1}{2}\left[\left(F_j\right)_{x_k}+\Lambda U_{x_k}\right]\\
\left(F_j\right)^-_{x_k}&=\frac{1}{2}\left[\left(F_j\right)_{x_k}-\Lambda U_{x_k}\right]
\end{aligned} \tag{54}$$

In our locally global Lax-Friedrichs approach, Λ is determined by Eq. (55). λ_i is a positive parameter chosen to be larger than the local maximum eigenvalues of the Jacobian $J = \partial F_j/\partial U$ on point i. In the temporal integral procedures of point I, Λ is the maximum of λ_i's of all the supporting points in the grid stencil centered on point I. Taking 1-D 2-2-2-2 scheme as an example, when the Euler equations are solved at the grid point I in the inner field, the largest λ_i of five neighboring points (I-2 < i < I+2) in the stencil is picked as Λ. On the next grid point, the procedure is repeated. Compared to using a constant Λ in the whole domain, the locally global Lax-Friedrichs approach has the benefit of maintaining low dissipation even though it's more computationally expensive.

$$\Lambda=\max\left(\lambda_i\right) \tag{55}$$

In this paper, two-dimensional Euler equations are solved by the new scheme. A rectangular domain is used for simulations and periodic boundary conditions are set for all the test case. Because there is no physical boundary in the domain, uniform grid points are used for simplicity and no boundary closure schemes is required. The discretization is performed in physical domain directly with the schemes. If the domain is non-rectangular, which is a more general case, the curvilinear coordinates can be used in the physical domain and a coordinate transform between physical and computational domain is needed. Then the schemes are applied in the computational domain.

1-D Convective Flow

The first test for Euler equations is the 1-D convective flow in x direction. Same test case is used in Qiu & Shu's paper [23]. The initial condition (t=0) and exact solution is given by Eq. (56). Since the perturbation is only in density, the exact solution corresponds to a passive convection of the initial density perturbation.

$$\begin{aligned} \rho(x,t) &= 1 + 0.2\sin(\pi(x-t)) \\ u(x,t) &= 1 \\ p(x,t) &= 1 \end{aligned} \tag{56}$$

The computational domain is in a range of $0 < x < 2$, which is one period in wave length. N+1 grid points are distributed uniformly and periodic boundary conditions on both sides are used. Same as the calculation of wave equation, 4th-order Runge-Kutta scheme are applied to time integral and both central and upwind schemes on three different centered stencils (1-1-1-1, 2-2-1-1 and 2-2-2-2) are tested. For 1-1-1-1 and 2-2-1-1 schemes, CFL number is set as 0.1; for 2-2-2-2 scheme, CFL number is 0.05. Both is small enough to make the error dominated by spatial discretization in the numerical results.

The errors of density between numerical solution and exact solution after running for one period (t = 2.0) are given in Table 7, Table 8, and Table 9. The order is estimated based on grid refinements. Results of central scheme (α = 0) and upwind scheme ($\alpha \neq 0$) on a same stencil are compared. Grid refinement results show that all schemes achieve or surpass the expected orders except when error is less than 10^{-12}, where machine error may affect the results in some cases. For the upwind scheme, the error is larger than that of central scheme on a same stencil. This is reasonable because more damping is introduced in upwind scheme which lowers accuracy. Despite the fact that the central scheme doesn't have numerical dissipation, the simulation is still stable and even more accurate because of the stabilization effect of RK-4.

Table 7. Errors and rates of convergence of 1-1-1-1 scheme for 1-D convective flow.

N	1-1-1-1 scheme, α = 0				1-1-1-1 scheme, α = 1.5			
	L_1 error	Order	L_∞ error	Order	L_1 error	Order	L_∞ error	Order
5	2.23E-03	\	3.16E-03	\	1.03E-02	\	1.53E-02	\
10	1.27E-04	4.14	1.87E-04	4.08	6.81E-04	3.92	1.01E-03	3.92
20	7.42E-06	4.10	1.14E-05	4.03	4.40E-05	3.95	6.66E-05	3.92
40	4.57E-07	4.02	7.10E-07	4.01	2.74E-06	4.01	4.23E-06	3.98
80	2.84E-08	4.01	4.43E-08	4.00	1.70E-07	4.01	2.66E-07	3.99

Table 8. Errors and rates of convergence of 2-2-1-1 scheme for 1-D convective flow.

N	2-2-1-1 scheme, α = 0				2-2-1-1 scheme, α = -1			
	L_1 error	Order	L_∞ error	Order	L_1 error	Order	L_∞ error	Order
5	2.07E-04	\	2.93E-04	\	3.78E-04	\	5.77E-04	\
10	2.98E-06	6.12	4.38E-06	6.06	9.90E-06	5.26	1.54E-05	5.23
20	4.53E-08	6.04	6.90E-08	5.99	2.44E-07	5.34	3.83E-07	5.33
40	7.05E-10	6.01	1.09E-09	5.99	4.96E-09	5.62	7.73E-09	5.63
80	1.10E-11	6.01	1.87E-11	5.86	8.61E-11	5.85	1.35E-10	5.84

Table 9. Errors and rates of convergence of 2-2-2-2 scheme for 1-D convective flow.

N	2-2-2-2 scheme, $\alpha = 0$				2-2-2-2 scheme, $\alpha = 12$			
	L_1 error	Order	L_∞ error	Order	L_1 error	Order	L_∞ error	Order
5	1.24E-05	\	1.75E-05	\	6.72E-05	\	1.04E-04	\
10	4.95E-08	7.97	7.29E-08	7.91	3.83E-07	7.45	5.78E-07	7.49
20	1.89E-10	8.04	2.90E-10	7.97	1.66E-09	7.86	2.56E-09	7.82
40	1.28E-12	7.21	2.57E-12	6.82	7.07E-12	7.87	1.10E-11	7.86
80	2.81E-12	-1.14	3.57E-12	-0.48	6.78E-14	6.70	1.45E-13	6.24

2-D Convective Flow

The 2nd test is the 2-D convective flow in an arbitrary direction. The initial condition (t=0) and exact solution is given by Eq. (57). Just like 2-D Fourier analysis in chapter II, there is an angle between the wave vector and mean flow velocity. The exact solution of 2-D convective flow is still a passive convection same as 1-D convective flow. Only density changes in the convection and the convection direction is aligned with mean flow velocity.

$$\begin{aligned} \rho(x,y,t) &= 1 + 0.2\sin(\pi(x+y-(u+v)t)) \\ u(x,y,t) &= 0.7 \\ v(x,y,t) &= 0.3 \\ p(x,y,t) &= 1 \end{aligned} \tag{57}$$

The computational domain is a square field in $0 < x < 2$ and $0 < y < 2$, which is one wave length in both direction. (N+1)×(N+1) grid points are distributed uniformly and periodic boundary conditions on all boundaries are used. 4th-order Runge-Kutta scheme are applied to time integral and CFL number is set as 0.1. Both central and upwind schemes on three different centered stencils (1-1-1-1, 2-2-1-1 and 2-2-2-2) are tested.

Same as 1-D convective flow simulation, the errors between numerical solution and exact solution at t = 2.0 are given in Table 10, Table 11, and Table 12. The magnitude of the errors is about one order higher than the 1-D simulation, which is caused by the anisotropy errors of numerical schemes. Grid refinement results show that all the schemes achieve or surpass the expected orders. Different from the 1-D convective flow results, it is observed that the upwind schemes have smaller errors and higher estimated orders than central schemes on the same stencils. In the results of 2-2-2-2 scheme, the accuracy is almost one order higher compared to central scheme. This phenomenon is probably due to the aliasing error in multidimensional simulation.

Table 10. Errors and rates of convergence of 1-1-1-1 scheme for 2-D convective flow.

N	1-1-1-1 scheme, $\alpha = 0$				1-1-1-1 scheme, $\alpha = 1.5$			
	L_1 error	Order	L_∞ error	Order	L_1 error	Order	L_∞ error	Order
5×5	1.78E-02	\	1.78E-02	\	1.41E-02	\	1.41E-02	\
10×10	1.31E-03	3.77	1.31E-03	3.77	7.66E-04	4.20	7.66E-04	4.20
20×20	8.36E-05	3.97	8.36E-05	3.97	4.47E-05	4.10	4.47E-05	4.10
40×40	5.27E-06	3.99	5.27E-06	3.99	2.74E-06	4.03	2.74E-06	4.03
80×80	3.29E-07	4.00	3.29E-07	4.00	1.70E-07	4.01	1.70E-07	4.01

Table 11. Errors and rates of convergence of 2-2-1-1 scheme for 2-D convective flow.

N	2-2-1-1 scheme, $\alpha = 0$				2-2-1-1 scheme, $\alpha = -1$			
	L_1 error	Order	L_∞ error	Order	L_1 error	Order	L_∞ error	Order
5×5	5.09E-03	\	5.09E-03	\	4.73E-03	\	4.73E-03	\
10×10	7.98E-05	6.00	7.98E-05	6.00	7.55E-05	5.97	7.55E-05	5.97
20×20	1.23E-06	6.02	1.23E-06	6.02	1.08E-06	6.13	1.08E-06	6.13
40×40	1.91E-08	6.00	1.91E-08	6.00	1.27E-08	6.41	1.27E-08	6.41
80×80	2.97E-10	6.01	2.97E-10	6.01	1.37E-10	6.53	1.37E-10	6.53

Table 12. Errors and rates of convergence of 2-2-2-2 scheme for 2-D convective flow.

N	2-2-2-2 scheme, $\alpha = 0$				2-2-2-2 scheme, $\alpha = 12$			
	L_1 error	Order	L_∞ error	Order	L_1 error	Order	L_∞ error	Order
5×5	1.14E-03	\	1.14E-03	\	8.13E-04	\	8.13E-04	\
10×10	5.30E-06	7.74	5.30E-06	7.74	2.06E-06	8.63	2.06E-06	8.63
20×20	2.09E-08	7.99	2.09E-08	7.99	4.76E-09	8.76	4.76E-09	8.76
40×40	8.74E-11	7.90	8.74E-11	7.90	1.60E-11	8.21	1.60E-11	8.21
80×80	2.32E-12	5.23	2.32E-12	5.24	4.33E-13	5.21	4.33E-13	5.21

1-D Acoustic Wave

In computational aeroacoustics, one of the main challenges is the accurate prediction of unsteady disturbance wave in long distance propagation. Small dissipation and dispersion are required at the same time to insure the high fidelity of sound wave in the simulation. As a test case for computational aeroacoustics, one-dimensional acoustic wave propagation is simulated with the new schemes. The initial conditions are given by Eq. (58). The air in standard atmosphere pressure and room temperature is used. A cosine wave is added to the static air flow field as the initial perturbation. The magnitude of initial perturbation wave in velocity and density is ε. Perturbation in pressure is determined by isentropic relation. To be general, the wave length of perturbations in velocity and density are different.

$$\begin{aligned}
&\Delta u = \varepsilon a_\infty \cos(\omega x), \quad u_\infty = 0\left[m/s\right] \\
&\Delta \rho = \varepsilon \rho_\infty \cos(2\omega x), \quad \rho_\infty = 1.1771\left[kg/m^3\right] \\
&\Delta p = \frac{\gamma p_\infty}{\rho_\infty}\Delta\rho, \qquad p_\infty = 101325\left[Pa\right] \\
&a_\infty = \sqrt{\gamma \frac{p_\infty}{\rho_\infty}}, \\
&\gamma = 1.4, \quad \omega = 6\pi, \quad \varepsilon = 10^{-5}
\end{aligned} \tag{58}$$

When the magnitude of disturbance is small enough, the flow is linear and an analytical solution given by Eq. (59) can be derived from acoustic wave equation as follows, where all the flow properties are the summation of mean flow values and small perturbations. The perturbations contain left-running wave and right-running wave components. This analytical solution is only valid for small perturbations.

$$\begin{aligned}
\rho(x,t) &= \rho_\infty + \frac{\varepsilon\rho_\infty}{2}[\cos(2\omega(x-a_\infty t)) + \cos(\omega(x-a_\infty t)) + \cos(2\omega(x+a_\infty t)) - \cos(\omega(x+a_\infty t))] \\
u(x,t) &= \frac{\varepsilon a_\infty}{2}[\cos(2\omega(x-a_\infty t)) + \cos(\omega(x-a_\infty t)) - \cos(2\omega(x+a_\infty t)) + \cos(\omega(x+a_\infty t))] \\
p(x,t) &= p_\infty + \frac{\gamma\varepsilon p_\infty}{2}[\cos(2\omega(x-a_\infty t)) + \cos(\omega(x-a_\infty t)) + \cos(2\omega(x+a_\infty t)) - \cos(\omega(x+a_\infty t))]
\end{aligned} \tag{59}$$

The original Euler equations are solved in a periodic domain of one wave length. The computational domain is in a range of $0 < x < 1/3$, which is one period in wave length of velocity perturbation. N+1 grid points are distributed uniformly and periodic boundary conditions on both sides are used. 4th-order Runge-Kutta scheme are applied to time integral and CFL number is set as 0.1 to reduce temporal errors. 1-1-1-1 and 2-2-2-2 upwind schemes with recommended α values are used for spatial discretization.

Firstly, short time calculation (t = 0.01s) are conducted to estimate the rate of convergence based on density. Because the analytical solution given in Eq. (59) is not the exact solution of Euler equations, three sets of numerical results are used in grid refinement to evaluate the accuracy. Table 13 shows the errors and rates of convergence of both 1-1-1-1 and 2-2-2-2 upwind schemes. Grid refinement results show that both of them can achieve the expected order (three for 1-1-1-1 and seven for 2-2-2-2) except when grid is too coarse or error goes to machine error level.

Table 13. Errors and rates of convergence of 1-1-1-1 & 2-2-2-2 scheme for acoustic wave.

N	1-1-1-1 scheme, α = 1.5				2-2-2-2 scheme, α = 12			
	L_1 error	Order	L_∞ error	Order	L_1 error	Order	L_∞ error	Order
5	0.00E+00	\	0.00E+00	\	0.00E+00	\	0.00E+00	\
10	3.47E-07	\	6.24E-07	\	4.20E-06	\	5.95E-06	\
20	4.14E-06	-3.58	6.10E-06	-3.29	4.11E-08	6.68	6.35E-08	6.55
40	6.38E-07	2.70	9.81E-07	2.64	3.11E-10	7.04	4.93E-10	7.01
80	4.52E-08	3.82	7.18E-08	3.77	3.25E-12	6.58	5.14E-12	6.58
160	2.80E-09	4.01	4.47E-09	4.00	4.76E-13	2.77	6.49E-13	2.99

To assess the performance of the numerical scheme on capturing the unsteady acoustic wave in long distance, longer time simulations are conducted. Errors of 2-2-2-2 upwind scheme are compared in Figure 24 at different time (t=0.01s, 0.1s, 1.0s), which corresponds to traveling about 1, 10, and 100 wave length. Three different sets of grids (N = 10, 20, 40) are used to show the growth of error. Both the L_1 error (the average deviation) and the L_∞ error (the maximum deviation) present an approximately linear growth along with simulation time. The straight lines indicate the order of accuracy is maintained during simulation. No exponential behavior is observed which means the error will not be amplified in long time simulation. In other words, the growth of error is the result of accumulation of temporal error in time integral.

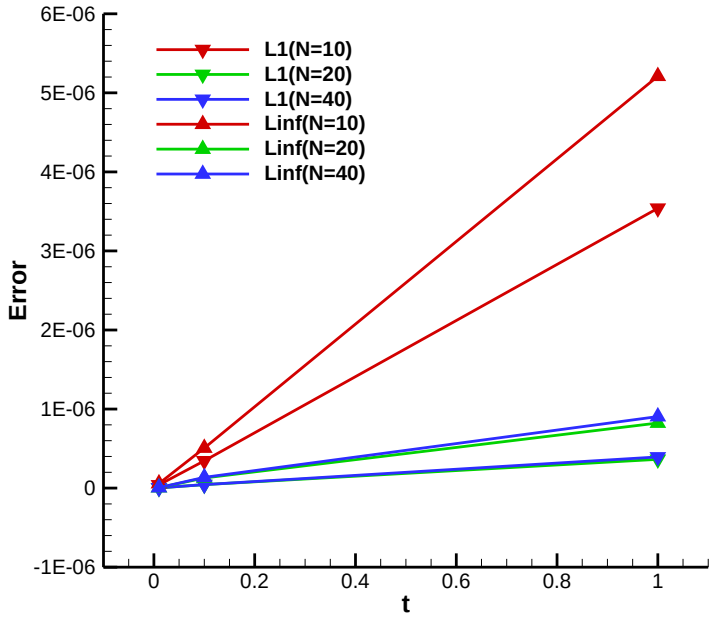

Figure 24. Growth of error with simulation time for 2-2-2-2 scheme.

Figure 25 shows the density distributions from simulation on when 21 grid points (N = 20) are used. It shows that at different simulation time, good agreement between the numerical results and analytical solution is maintained and there is no big deviation in both phase and amplitude of the acoustic wave. The discrepancy mainly appears near the peaks. In fact, we observe the same level deviation when N is increased to 40 or 80, which implies the difference is mainly due to the inherent error of the linearization for analytical solution. Same analysis can be done with 1-1-1-1 scheme and similar behavior can be observed.

In summary, the proposed very high-order upwind multilayer compact scheme is able to maintain very small dispersive error and dissipation at the same time. The error shows a linear grows along with simulation time and the spatial discretization error is not amplified in long time simulation. So it's appropriate for aeroacoustic simulation.

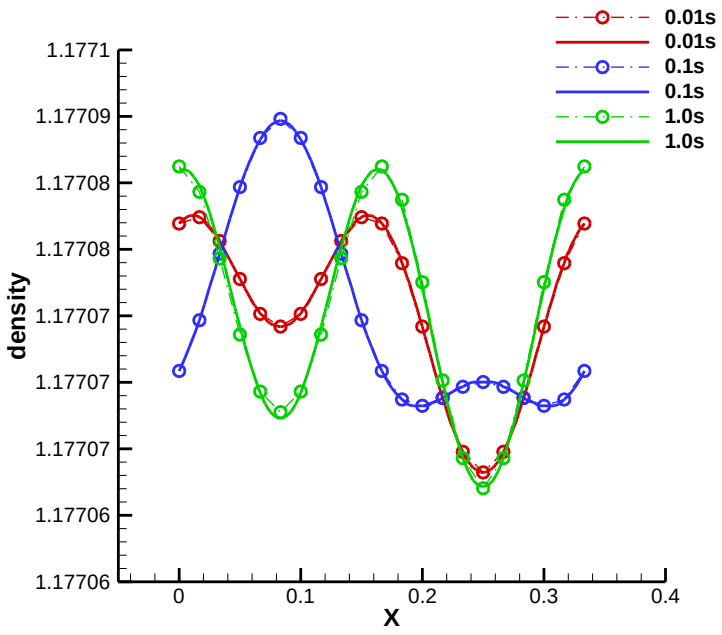

Figure 25. Density distribution at different simulation time for 2-2-2-2 scheme.

2-D Isentropic Vortex

To show the performance of the proposed numerical scheme on capturing vortical flows, the 2-D inviscid isentropic vortex in a uniform mean flow is tested. Similar test cases have also been by Mundis & Edoh [27, 28]. An rectangular domain and uniform grids are used to simulate the 2-D vortex. The uniform flow conditions are set as follows:

$$
\begin{aligned}
& p_\infty = 101325\left[Pa\right],\ \ T_\infty = 300\left[K\right],\ \ \rho_\infty = \frac{p_\infty}{RT_\infty} \\
& a_\infty = \sqrt{\gamma RT_\infty},\qquad M = \frac{u_\infty}{a_\infty} \\
& \gamma = 1.4,\qquad\qquad R = 286.94\left[J\cdot kg^{-1}\cdot K^{-1}\right]
\end{aligned}
\tag{60}
$$

where Mach number are set to 0 for stationary vortex and 0.5 for convective vortex, respectively. An isentropic perturbation is added to the uniform mean flow as the initial condition, which is given in Eq. (61). The perturbation occurs in both x and y velocity components, temperature and pressure. The vortex is located at (x_0, y_0) and r is the distance to its center. The strengths of perturbations have the maximal value at the vortex core and decay in radical direction. Only velocity and temperature perturbations need to be defined independently in Eq. (61). Pressure and density can be determined by isentropic relations. The amplitude of the perturbation in density is about 3.34% of the mean flow value. The vortex edge is defined at the location where perturbation in density is 0.1% of vortex core strength. For the case in this paper, vortex width is about 2.26m. The exact solution of this problem is a passive convection with the mean flow and the vortex should maintain its structure during the convection. It's an appropriate test case to show the ability of numerical scheme in terms of vortex preservation, which depends on the dissipation and dispersion of a scheme, and anisotropy error as well.

$$\delta u = -\frac{\sqrt{RT_\infty}}{2\pi}\left(y-y_0\right)e^{1-r^2},\quad \delta v = \frac{\sqrt{RT_\infty}}{2\pi}\left(x-x_0\right)e^{1-r^2}$$
$$\delta T = -T_\infty \frac{\gamma-1}{16\gamma\pi^2}e^{2\left(1-r^2\right)}, \tag{61}$$
$$\frac{\delta p}{p_\infty} = \gamma\frac{\delta\rho}{\rho_\infty} = \frac{\gamma}{\gamma-1}\frac{\delta T}{T_\infty},$$

The computational domain is a square field in $0 < x < L$ and $0 < y < L$ and vortex core is located at the center of the square. (N+1)×(N+1) grid points are distributed uniformly. Periodic boundary conditions are set on all boundaries. L has a value of 22.0m which is about ten times of the vortex width. This domain is large enough to reduce the boundary effects because the initial perturbations on the computational boundaries are negligible. 1-1-1-1 and 2-2-2-2 upwind schemes with recommended α values are applied to the 2-D isentropic vortex simulation. 4th-order Runge-Kutta scheme is used for time integral and CFL number is set as 0.1 to reduce temporal errors.

Similar to the previous case of 1-D acoustic wave, the short time simulation (t = 0.01s) is conducted to estimate the rate of convergence firstly. Both the stationary vortex (M = 0) and convective vortex (M = 0.5) are tested. Table 14 and Table 15 show the accuracy estimation based on density. All simulations show that both 1-1-1-1 scheme (3rd-order) and 2-2-2-2 scheme (7th-order) can achieve or surpass the expected order. The simulation for stationary vortex is more accurate than convective vortex. Comparing Table 14 and Table 15, we can find that the errors are smaller and estimated orders are higher for stationary vortex, especially when N is large. For the cases of N = 160 and 320, the errors of convective vortex are one order greater than those of stationary vortex, indicating that convective vortex is harder to be accurately captured by the new schemes.

Table 14. Errors and rates of convergence of 1-1-1-1 & 2-2-2-2 scheme for stationary vortex (M = 0).

N	1-1-1-1 scheme, α = 1.5				2-2-2-2 scheme, α = 12			
	L_1 error	Order	L_∞ error	Order	L_1 error	Order	L_∞ error	Order
20	0.00E+00	\	0.00E+00	\	0.00E+00	\	0.00E+00	\
40	1.58E-03	\	1.58E-03	\	1.46E-03	\	1.46E-03	\
80	1.49E-04	3.40	1.49E-04	3.40	5.45E-05	4.75	5.45E-05	4.75
160	8.02E-06	4.22	8.02E-06	4.22	3.27E-07	7.38	3.27E-07	7.38
320	3.60E-07	4.48	3.60E-07	4.48	8.72E-10	8.55	8.72E-10	8.55

Table 15. Errors and rates of convergence of 1-1-1-1 & 2-2-2-2 scheme for convective vortex (M = 0.5).

N	1-1-1-1 scheme, α = 1.5				2-2-2-2 scheme, α = 12			
	L_1 error	Order	L_∞ error	Order	L_1 error	Order	L_∞ error	Order
20	0.00E+00	\	0.00E+00	\	0.00E+00	\	0.00E+00	\
40	1.50E-03	\	1.24E-03	\	1.44E-03	\	1.34E-03	\
80	2.14E-04	2.81	1.73E-04	2.84	6.56E-05	4.46	5.94E-05	4.50
160	1.80E-05	3.57	1.29E-05	3.75	5.96E-07	6.78	5.57E-07	6.74
320	1.10E-06	4.03	9.31E-07	3.79	3.36E-09	7.47	2.64E-09	7.72

After investigating the accuracy of the schemes, long time simulation results at t = 1.267s are analyzed, which corresponds a time period after the vortex has traveled about 10 times of its diameter in the case of M = 0.5. In Figure 26 and Figure 27, the vorticity distribution in stationary and convective vortex along the centerline (y = 11m) are given respectively. The reduce of both dissipative and dispersive errors is clear when grid points increase. For 1-1-1-1 upwind scheme, resolution with 161×161 grid points (N=160) is accurate enough while resolution with 81×81 grid points (N=80) achieve about the same level accuracy in 2-2-2-2 upwind scheme. In both stationary and convective vortex, the peak of vorticity is underestimated when girds resolution is not enough. The peak of the wave corresponds to the high frequency wave mode. Due to the dissipation in large wave number region as shown in Fourier analysis in chapter II, the new schemes will underestimate the value at the peak. For convective vortex case, a discrepancy of vortex position exists when resolution is not good enough. This is related to dispersion or anisotropy error from numerical simulations. While for stationary vortex, no such deviation is observed.

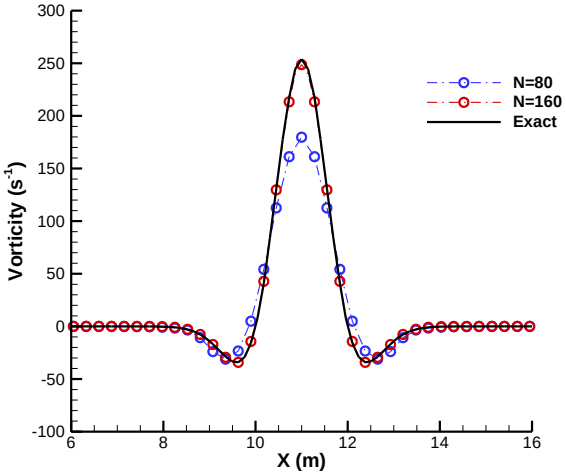

a), 1-1-1-1 upwind scheme

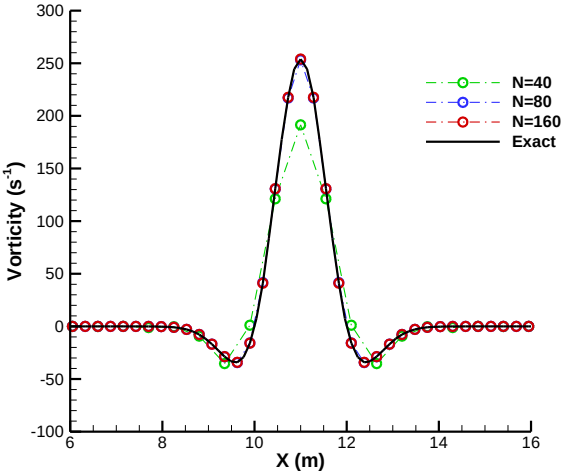

b), 2-2-2-2 upwind scheme

Figure 26. Vorticity distribution on a centerline in x direction for stationary vortex (t = 1.267s).

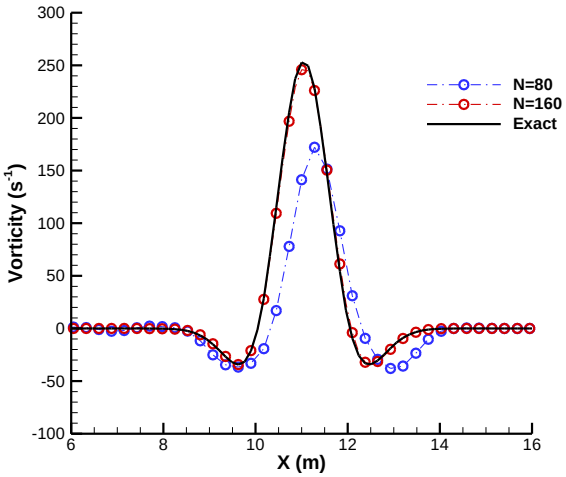

a), 1-1-1-1 upwind scheme

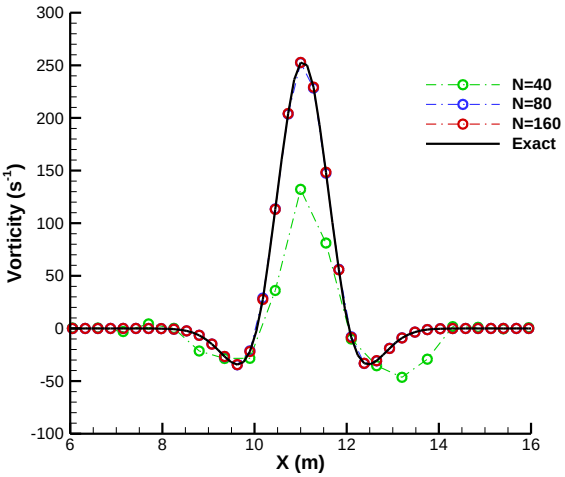

b), 2-2-2-2 upwind scheme

Figure 27. Vorticity distribution on a centerline in x direction for convective vortex (t = 1.267s).

To investigate the anisotropy error, Figure 28 and Figure 29 show the density contour in a plane for stationary vortex and convective vortex respectively. All results come from the simulation with 161×161 grid points (N=160) to provide enough resolution for the contour plots. The exact solution of this problem should have perfect isotropic distribution in density, which means the contour lines should be concentric circles. We After running for one convection period, both 1-1-1-1 and 2-2-2-2 upwind scheme show a good isotropic distribution in terms of density perturbation.

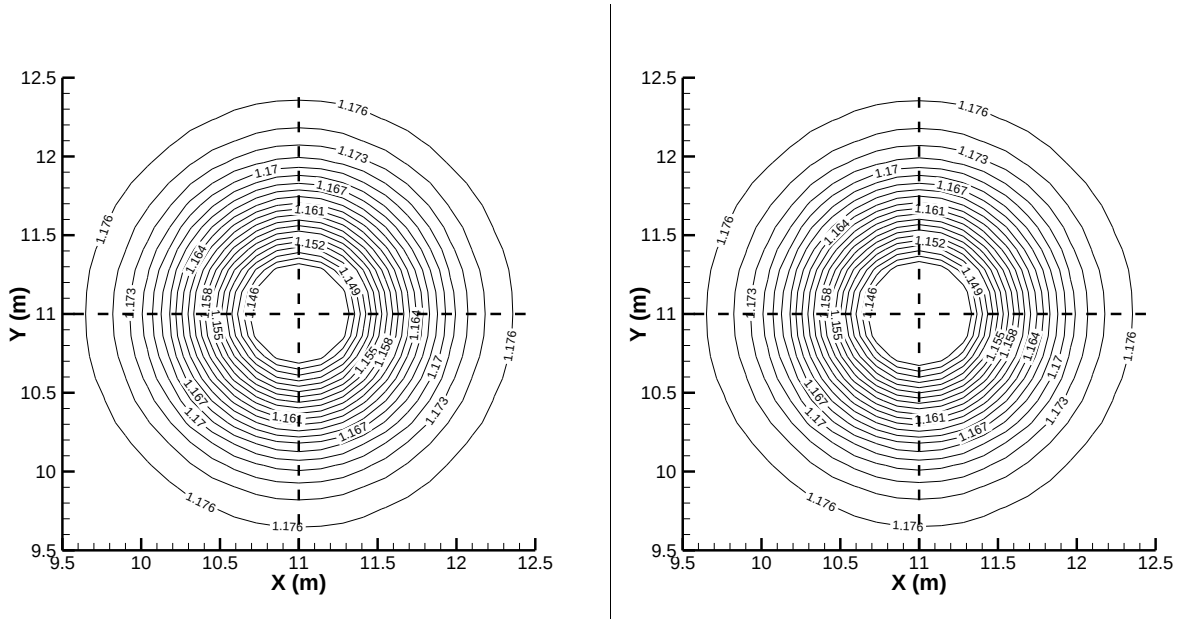

a), 1-1-1-1 upwind scheme b), 2-2-2-2 upwind scheme

Figure 28. Density contour in a plane for stationary vortex (t = 1.267s).

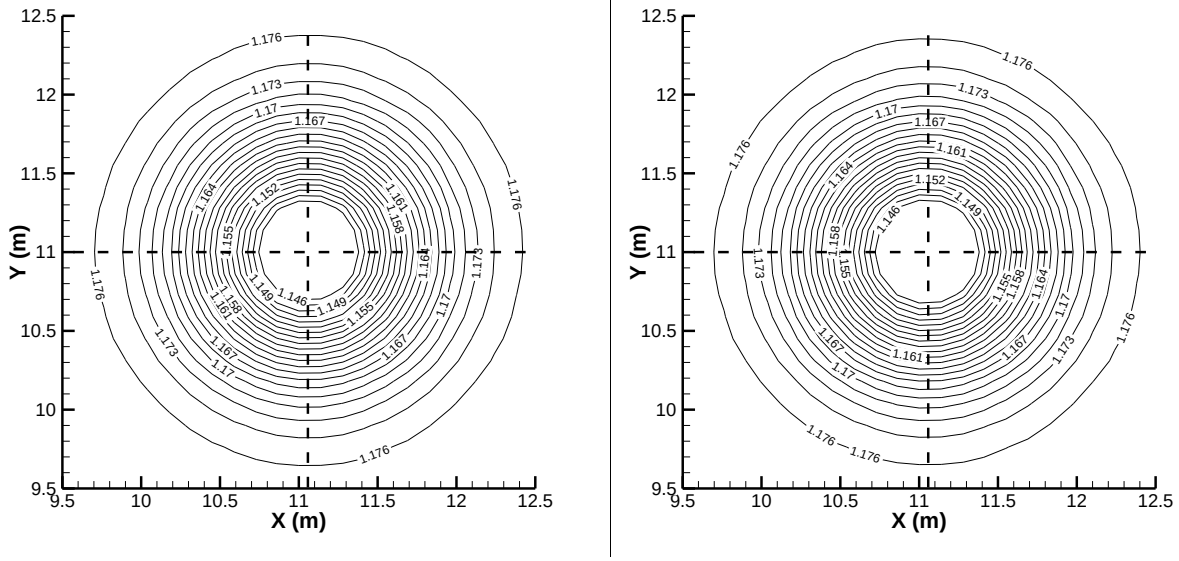

a), 1-1-1-1 upwind scheme b), 2-2-2-2 upwind scheme

Figure 29. Density contour in a plane for convective vortex (t = 1.267s).

Figure 30 shows the density distribution along the lines passing the vortex core. θ is the angle between x-axis and the line. Two different θ of values 0 and 45 are used in order to show the anisotropy error, which corresponds to two lines in different orientations. The results of 1-1-1-1 scheme and 2-2-2-2 scheme show that the density distributions on two lines are similar and the deviations from exact solution are both very small except at the peak, which means the new schemes have good isotropy property. This observation is consistent with Figure 29. In the approximation of cross derivative, our multilayer schemes take into information from neighboring points in different orientations while conventional finite difference methods only do approximation in one direction. Thus, it has the advantage to overcome anisotropy error.

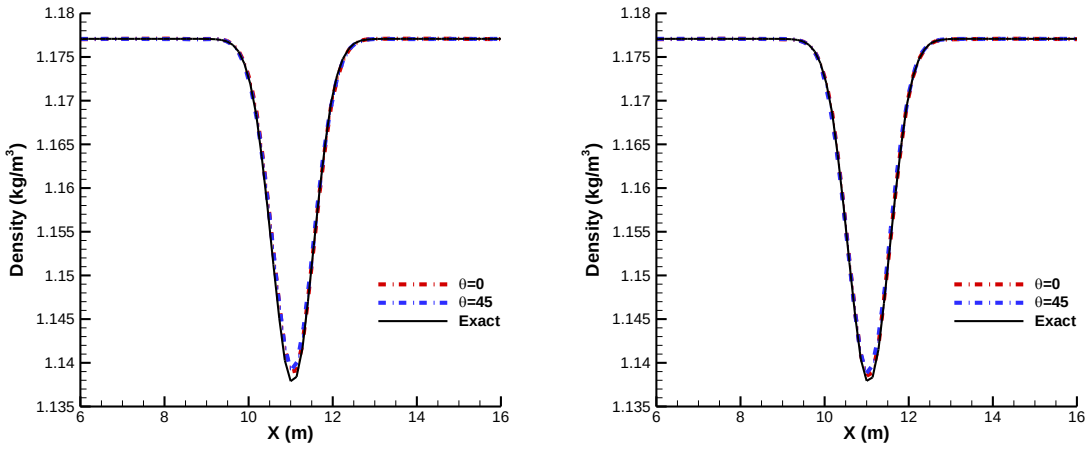

a), 1-1-1-1 upwind scheme b), 2-2-2-2 upwind scheme

Figure 30. Density distribution along a centerline in different direction (θ = 0 and θ = 45).

C. Compressible Navier-Stokes Equations

The governing equations for the DNS of compressible viscous flow is the three-dimensional Navier-Stokes equations, which can be written in the following conservation-law form in the Cartesian coordinates,

$$\frac{\partial U}{\partial t}+\frac{\partial F_j}{\partial x_j}+\frac{\partial F_{vj}}{\partial x_j}=0 \tag{62}$$

where U, F_j, and F_{vj} are the vectors of flow variables, convective flux, and viscous flux in the jth spatial direction respectively. U and F_j are the same as in Euler equations and F_{vj} is given as follows,

$$F_{vj}=\begin{bmatrix} 0 \\ \tau_{1j} \\ \tau_{2j} \\ \tau_{3j} \\ \tau_{kj}u_k+q_j \end{bmatrix} \tag{63}$$

where τ_{ij} is the viscous stress and it can be calculated by Eq. (64), λ is the second viscous coefficient which is assumed to be $-2\mu/3$. μ is calculated by Sutherland's law in the form of Eq. (65). q_j is the heat flux calculated by Eq. (66). The heat conductivity coefficient κ is computed from a constant Prandle number $Pr = 0.72$.

$$\tau_{ij}=-\mu\left(\frac{\partial u_i}{\partial x_j}+\frac{\partial u_j}{\partial x_i}\right)-\lambda\frac{\partial u_k}{\partial x_k}\delta_{ij} \tag{64}$$

$$\mu=\mu_r\left(\frac{T}{T_0}\right)^{3/2}\frac{T_r+T_s}{T+T_s} \tag{65}$$

$$q_j=-\kappa\frac{\partial T}{\partial x_j} \tag{66}$$

Using the same methodology for Euler equations, the auxiliary equations for compressible N-S Equations can be derived. Different from inviscid flux, the central scheme should be applied due to the elliptic property of the

viscous terms. It should be noticed that the multilayer compact scheme are applied twice in the approximation of viscous terms because the second and cross derivatives of velocity and temperature will appear in the first derivatives $(F_{vj})_x$, $(F_{vj})_y$.

For wall bounded flows governed by Navier-Stokes equations, non-slip boundary conditions are applied to the walls. Non-slip means there is no relative motion between wall and the neighboring fluid particles, i.e., $u = U_{wall}$. If the wall is static, the fluid velocity at wall is zero. Two types of boundary conditions for temperature can be used, 1) isothermal wall; 2) adiabatic wall. For isothermal case, wall temperature is a constant value in simulation; for adiabatic case, the gradient of temperature at wall is set to be zero in simulation.

Steady Supersonic Couette Flow

Couette flow is a shear flow bounded by two parallel walls. Supersonic compressible Couette flow is an appropriate testing case for Navier-Stokes calculation because of its simplicity in solution. While steady solutions are 1-D functions of wall-normal distance y, unsteady Couette flows are 2-D or 2-D transient flows if disturbances exist. The steady solution is easy to get by a shooting methods and the unsteady solution under small disturbance can be generated by linear stability theory (LST). Details can be found in Ref. [26]. In this paper, only the steady simulation is performed as a test case for Navier-Stokes simulations.

In this paper, the bottom wall is static and adiabatic and the top wall is moving in a constant velocity U_∞ and has constant temperature T_∞. The flow conditions are given in Eq. (67). Reynolds number is small to maintain Laminar and stable flow in the channel.

$$\begin{aligned} &M_\infty = 2, \quad \mathrm{Re}_\infty = 100 \\ &T_\infty = 300[\mathrm{K}], \; p = 101325[Pa], \; T_w = T_r \end{aligned} \tag{67}$$

The exact solution of steady Couette flow can be derived in implicit form as follows,

$$U_\infty \int_0^{u^*} \mu_{ref} \left(\frac{T_\infty}{T_{ref}}\right)^{1.5} \left(\frac{T(u^*)}{T_\infty}\right)^{1.5} \left(\frac{T_{ref}+T_s}{T(u^*)+T_s}\right) du^* = \tau_w y \tag{68}$$

$$T(u^*) = T_\infty \left[1 + \left(\frac{T_w - T_r}{T_\infty}\right)(1-u^*) + \frac{(\gamma-1)}{2}\mathrm{Pr}\, M_\infty^2 \left(1-(u^*)^2\right)\right] \tag{69}$$

where $u^* = u/U_\infty$ is the non-dimensional velocity, the variables with ∞ subscript represent flow conditions on the top wall, T is temperature which is a function of u^*, y is the height from the bottom wall, τ_w is wall shear stress and it's a fixed value in Couette flow. Eq. (72) gives the way to calculate the value, in which H is the height of the channel and can be calculated from Reynolds number. T_r is recovery temperature and T_w is wall temperature, in adiabatic case they are equivalent. Viscosity μ is calculated by Sutherland's law from temperature. The constants with "*ref*" subscript are the reference constants in Sutherland's law which are given in Eq. (73). Prandtl number (Pr) is 0.72, γ is 1.4 and gas constant R is 286.94 $[m^2 \cdot s^{-2} \cdot K^{-1}]$.

$$T_r = T_\infty \left[1 + \frac{(\gamma-1)}{2}\mathrm{Pr}\, M_\infty^2\right] \tag{70}$$

$$U_\infty = M_\infty \sqrt{\gamma R T_\infty} \tag{71}$$

$$\tau_w = \frac{U_\infty}{H} \int_0^1 \mu_{ref} \left(\frac{T_\infty}{T_{ref}}\right)^{1.5} \left(\frac{T(u^*)}{T_\infty}\right)^{1.5} \left(\frac{T_{ref}+T_s}{T(u^*)+T_s}\right) du^* \tag{72}$$

$$\mu_{ref} = 1.7894 \times 10^{-5} \left[\frac{kg}{m \cdot s}\right], \quad T_{ref} = 288[K], \quad T_s = 110.3333[K] \tag{73}$$

The computational domain is a rectangular field in $0 < x < L$ and $0 < y < H$. The length L in x direction is arbitrary for steady simulations because each x location is equivalent. 7 grid points in x direction and (N+1) grid points in y direction are distributed uniformly. Periodic boundary conditions are set on inlet and outlet, and non-slip

and isothermal wall conditions are applied on bottom and top walls. It needs to be noticed that although the physical temperature condition for bottom wall is adiabatic, isothermal temperature can still be used because the flow is steady. 1-1-1-1 and 2-2-2-2 upwind schemes with recommended α values are applied to the 2-D steady Couette flow simulations. Zhong's 5th-order upwind scheme[25] is also applied as a comparison. 3rd-order Runge-Kutta scheme is used for time integral.

Firstly, Figure 31 shows the non-dimensional temperature T^* and velocity u^* distribution obtained by the 2-2-2-2 scheme on a mesh with only 7 grid points (N = 6). Very good agreement is obtained between the numerical and exact solution, this resolution with such coarse mesh is hard to achieve by conventional finite difference methods.

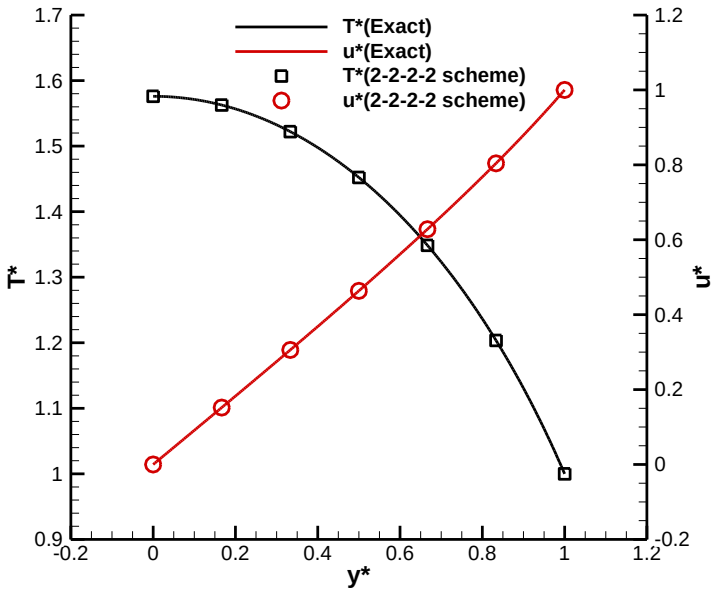

Figure 31. Temperature and velocity distribution for steady Couette flow in numerical results with 2-2-2-2 upwind compact scheme (N = 6).

To illustrate the high resolution and accuracy of our new schemes further, the numerical errors of Zhong's 5th-order scheme and the new 1-1-1-1 scheme, and 2-2-2-2 scheme are given in Table 16, Table 17, Table 18. It shows that all these schemes can reach the expected order of accuracy for Navier-Stokes calculation, which is 7 for 2-2-2-2 upwind scheme, 3 for 1-1-1-1 upwind scheme, and 5 for Zhong's explicit upwind scheme. Comparing the error on the same mesh, we can observe that 2-2-2-2 scheme shows the smallest errors on all mesh settings which is consistent with its 7th-order accuracy. Comparing Table 17 and Table 18, the 3rd-order 1-1-1-1 scheme shows smaller error than Zhong's 5th-order scheme when in the case of N = 8 are used, and their error are about the same for N = 16. For N = 32 and 64 cases, Zhong's 5th-order scheme is more accurate than 3rd-order 1-1-1-1 scheme.

The error analysis indicates that the new schemes with lower-orders can have better performance on coarse grids than conventional finite difference methods even with higher-orders. When the grid resolution is not fine enough, the accuracy of numerical results mainly depends on the resolving ability for large wave number components. Due to the spectral-like resolution, our multilayer compact schemes can have acceptable accuracy even with only few grid points. As a comparison, the performances of conventional finite difference methods like Zhong's 5th-order upwind scheme are not as good on coarse grids.

Table 16. Errors and rates of convergence of 2-2-2-2 scheme for steady supersonic Couette flow.

N	2-2-2-2 scheme, α = 12					
	L1 error	Order	L2 error	Order	L∞ error	Order
8	1.06E-06		1.25E-06		1.97E-06	
16	1.79E-08	5.88	2.22E-08	5.81	4.13E-08	5.57
32	1.12E-10	7.32	1.37E-10	7.35	3.52E-10	6.88
64	7.29E-13	7.27	8.99E-13	7.25	1.55E-12	7.82

Table 17. Errors and rates of convergence of 1-1-1-1 scheme for steady supersonic Couette flow.

N	1-1-1-1 scheme, α = 1.5					
	L1 error	Order	L2 error	Order	L∞ error	Order
8	7.77E-05		8.81E-05		1.28E-04	
16	7.82E-06	3.31	9.09E-06	3.28	1.42E-05	3.17
32	5.88E-07	3.73	7.07E-07	3.68	1.18E-06	3.59
64	4.05E-08	3.86	5.02E-08	3.81	8.78E-08	3.75

Table 18. Errors and rates of convergence of Zhong's 5th-order scheme for steady supersonic Couette flow.

N	Zhong's 5th-order, α = -6					
	L1 error	Order	L2 error	Order	L∞ error	Order
8	1.75E-04		2.07E-04		3.76E-04	
16	6.91E-06	4.66	8.60E-06	4.59	1.74E-05	4.43
32	2.59E-07	4.74	3.41E-07	4.66	8.60E-07	4.34
64	9.96E-09	4.70	1.38E-08	4.62	4.56E-08	4.24

IV.Conclusions

In this paper, a new very high-order upwind multilayer compact scheme is derived. The goal of the new scheme is to solve, with very high accuracy, flows containing very complex physics but over simple geometries. The multilayer idea refers to introducing first derivatives on the grid points and using both values and derivatives to construct finite difference schemes. As a result, the accuracy and resolution can be significantly improved. Specific conclusions are listed below.

(1) Fourier analysis results show that both the dissipation and dispersive error of the new scheme is much smaller compared to conventional finite difference methods (Zhong's explicit and compact scheme [25]). Due to increase of degrees of freedom, the resolution in large wave number region is notably improved even with a narrower stencil. Compared to DG methods, the resolving ability for very large wave number is weaker, but it has the advantage of more relaxed stability condition for time integral, and better simplicity and computational efficiency as well.

(2) Boundary stability analysis with eigenvalue spectrum shows that the stable boundary closure schemes can be easily derived with the benefits of compact stencils. The upwind coefficients play an important role in stabilizing the high-order boundary closure schemes. Like most finite difference schemes, high-order multilayer schemes have more severe boundary instability problem than low-order schemes. The 7th-order upwind scheme (2-2-2-2) with α = 12 is stable only when coupled with 6th-order boundary closure schemes on all boundary points and their adjacent points. The 3rd-order upwind scheme (1-1-1-1) with any positive α, even the 4th-order central scheme with α = 0, are stable when coupled with both 3rd and 2nd-order boundary closure schemes.

(3) Numerical experiments with various test cases in linear wave equation, Euler equations, and Navier-Stokes equations are simulated with our very high-order upwind multilayer compact scheme. Both 1-D and 2-D simulations are performed and 3-D simulation can follow the same methodology. The numerical solutions in all test cases are compared with analytical solutions and rates of convergence are evaluated by grid refinements. All the test cases indicate the expected order of accuracy and generate satisfying results on coarse meshes with very few grid points, which validate the spectral-like resolution. Particularly, the results of acoustic wave show the high fidelity for unsteady disturbance wave in long time propagation due to small dissipative and dispersive error; the results of 2-D isentropic vortex indicate good isotropy property of the new numerical schemes; the results of steady supersonic Couette flow shows implementation of our new schemes on Navier-Stokes simulations is practicable, which is a good start for transient flows and hypersonic boundary layer simulations in the future.

In summary, the analysis and numerical experiments demonstrate that the proposed scheme is accurate and stable in a wide range of wave scales. When coupling with boundary closure schemes, the upwind setting has stabilization effect on the boundary instability. Various inviscid and viscous flow problems show the high accuracy of the new schemes for linear and nonlinear equations, and resolution can be significantly improved with narrow stencils and few grid points in mesh.

Future work on this research will include combination with shock-fitting methods for hypersonic flows, which is considered in Zhong's previous work [25]. Boundary layer stability, receptivity, and transition, which is summarized in [1], will also be investigated using the new very high-order upwind multilayer schemes.

Appendix

A. Formulas for Second Derivatives

1) Centered Stencils

1-1-2-2 Scheme

$$\begin{aligned} a_{i\pm1} &= \frac{24}{11} \pm \frac{3}{20}\alpha, \qquad a_i = -\frac{48}{11}, \\ b_{i\pm2} &= \pm\frac{1}{132} + \frac{1}{600}\alpha, \qquad b_{i\pm1} = \mp\frac{20}{33} - \frac{17}{300}\alpha, \qquad b_i = -\frac{19}{100}\alpha. \end{aligned} \tag{74}$$

α needs to be negative for upwind schemes.

2-2-1-1 Scheme

$$\begin{aligned} a_{i\pm2} &= \frac{1}{36} \pm \frac{1}{144}\alpha, \qquad a_{i\pm1} = \frac{20}{9} \pm \frac{7}{36}\alpha, \qquad a_i = -\frac{9}{2}, \\ b_{i\pm1} &= \mp\frac{2}{3} - \frac{1}{12}\alpha, \qquad b_i = -\frac{1}{4}\alpha. \end{aligned} \tag{75}$$

α needs to be negative for upwind schemes.

2) Bias Stencils

0-1-0-1 Scheme

$$\begin{aligned} a_i &= -6, \qquad a_{i+1} = 6, \\ b_i &= -4, \qquad b_{i+1} = -2. \end{aligned} \tag{76}$$

0-2-0-1 Scheme

$$\begin{aligned} a_i &= -\frac{17}{2}, \qquad a_{i+1} = 8, \qquad a_{i+2} = \frac{1}{2}, \\ b_i &= -5, \qquad b_{i+1} = -4. \end{aligned} \tag{77}$$

0-3-0-3 Scheme

$$\begin{aligned} a_i &= -\frac{97}{6}, \qquad a_{i+1} = 0, \qquad a_{i+2} = \frac{27}{2}, \qquad a_{i+3} = \frac{8}{3}, \\ b_i &= -\frac{22}{3}, \qquad b_{i+1} = -18, \quad b_{i+2} = -9, \qquad b_{i+3} = -\frac{2}{3}. \end{aligned} \tag{78}$$

0-4-0-3 Scheme

$$\begin{aligned} a_i &= -\frac{145}{8}, \qquad a_{i+1} = -8, \qquad a_{i+2} = 18, \qquad a_{i+3} = 8, \qquad a_{i+4} = \frac{1}{8}, \\ b_i &= -\frac{47}{6}, \qquad b_{i+1} = -24, \qquad b_{i+2} = -18, \qquad b_{i+3} = -\frac{8}{3}. \end{aligned} \tag{79}$$

1-0-1-0 Scheme

$$\begin{aligned} a_{i-1} &= 6, \qquad a_i = -6, \\ b_{i-1} &= 2, \qquad b_i = 4. \end{aligned} \tag{80}$$

1-1-2-1 Scheme

$$\begin{aligned} a_{i-2} &= \frac{1}{18}, \quad a_{i-1} = 3, \quad a_i = -\frac{9}{2}, \quad a_{i+1} = \frac{13}{9}, \\ b_{i-1} &= 1, \quad b_i = 1, \quad b_{i+1} = -\frac{1}{3}. \end{aligned} \tag{81}$$

1-2-1-2 Scheme

$$\begin{aligned} a_{i-1} &= \frac{28}{27}, \quad a_i = -\frac{11}{2}, \quad a_{i+1} = 4, \quad a_{i+2} = \frac{25}{54}, \\ b_{i-1} &= \frac{2}{9}, \quad b_i = -2, \quad b_{i+1} = -2, \quad b_{i+2} = -\frac{1}{9}. \end{aligned} \tag{82}$$

1-3-1-2 Scheme

$$\begin{aligned} a_{i-1} &= \frac{59}{72}, \quad a_i = -\frac{115}{18}, \quad a_{i+1} = \frac{9}{2}, \quad a_{i+2} = \frac{19}{18}, \quad a_{i+3} = \frac{1}{72}, \\ b_{i-1} &= \frac{1}{6}, \quad b_i = -\frac{8}{3}, \quad b_{i+1} = -3, \quad b_{i+2} = -\frac{1}{3}. \end{aligned} \tag{83}$$

2-0-1-0 Scheme

$$\begin{aligned} a_{i-2} &= \frac{1}{2}, \quad a_{i-1} = 8, \quad a_i = -\frac{17}{2}, \\ b_{i-1} &= 4, \quad b_i = 5. \end{aligned} \tag{84}$$

2-1-2-1 Scheme

$$\begin{aligned} a_{i-2} &= \frac{25}{54}, \quad a_{i-1} = 4, \quad a_i = -\frac{11}{2}, \quad a_{i+1} = \frac{28}{27}, \\ b_{i-2} &= \frac{1}{9}, \quad b_{i-1} = 2, \quad b_i = 2, \quad b_{i+1} = -\frac{2}{9}. \end{aligned} \tag{85}$$

2-1-1-1 Scheme

$$\begin{aligned} a_{i-1} &= \frac{63}{22}, \quad a_i = -\frac{48}{11}, \quad a_{i+1} = \frac{3}{2}, \\ b_{i-2} &= -\frac{1}{66}, \quad \mathrm{b}_{i-1} = \frac{19}{22}, \quad b_i = \frac{19}{22}, \quad b_{i+1} = -\frac{23}{66}. \end{aligned} \tag{86}$$

3-0-3-0 Scheme

$$\begin{aligned} a_{i-3} &= \frac{8}{3}, \quad a_{i-2} = \frac{27}{2}, \quad a_{i-1} = 0, \quad a_i = -\frac{97}{6}, \\ b_{i-3} &= \frac{2}{3}, \quad b_{i-2} = 9, \quad b_{i-1} = 18, \quad b_i = \frac{22}{3}. \end{aligned} \tag{87}$$

3-1-2-1 Scheme

$$a_{i-3}=\frac{1}{72},\quad a_{i-2}=\frac{19}{18},\quad a_{i-1}=\frac{9}{2},\quad a_i=-\frac{115}{18},\quad a_{i+1}=\frac{59}{72},$$
$$b_{i-2}=\frac{1}{3},\quad b_{i-1}=3,\quad b_i=\frac{8}{3},\quad b_{i+1}=-\frac{1}{6}. \tag{88}$$

4-0-3-0 Scheme

$$a_{i-4}=\frac{1}{8},\quad a_{i-3}=8,\quad a_{i-2}=18,\quad a_{i-1}=-8,\quad a_i=-\frac{145}{8},$$
$$b_{i-3}=\frac{8}{3},\quad b_{i-2}=18,\quad b_{i-1}=24,\quad b_i=\frac{47}{6}. \tag{89}$$

B. Formulas for Cross Derivatives

2-2-1-1 Scheme

$$\begin{aligned}\left(u_{xy}\right)_{i,j}=&\frac{1}{h^2}\left(\frac{1}{144}u_1-\frac{1}{144}u_5+\frac{5}{9}u_7-\frac{5}{9}u_9-\frac{5}{9}u_{17}+\frac{5}{9}u_{19}-\frac{1}{144}u_{21}+\frac{1}{144}u_{25}\right)\\&+\frac{1}{h}\left(\frac{1}{6}\left(u_x\right)_7+\frac{1}{6}\left(u_x\right)_9-\frac{1}{6}\left(u_x\right)_{17}-\frac{1}{6}\left(u_x\right)_{19}\right)+\frac{1}{h}\left(\frac{1}{6}\left(u_y\right)_7-\frac{1}{6}\left(u_y\right)_9+\frac{1}{6}\left(u_y\right)_{17}-\frac{1}{6}\left(u_y\right)_{19}\right)\\&+o\left(h^6\right)\end{aligned} \tag{90}$$

1-1-2-2 Scheme

$$\begin{aligned}\left(u_{xy}\right)_{i,j}=&\frac{1}{h^2}\left(\frac{6}{11}u_7-\frac{6}{11}u_9-\frac{6}{11}u_{17}+\frac{6}{11}u_{19}\right)\\&+\frac{1}{h}\left(-\frac{1}{528}\left(u_x\right)_1-\frac{1}{528}\left(u_x\right)_5+\frac{5}{33}\left(u_x\right)_7+\frac{5}{33}\left(u_x\right)_9-\frac{5}{33}\left(u_x\right)_{17}-\frac{5}{33}\left(u_x\right)_{19}+\frac{1}{528}\left(u_x\right)_{21}+\frac{1}{528}\left(u_x\right)_{25}\right)\\&+\frac{1}{h}\left(-\frac{1}{528}\left(u_y\right)_1+\frac{1}{528}\left(u_y\right)_5+\frac{5}{33}\left(u_y\right)_7-\frac{5}{33}\left(u_y\right)_9+\frac{5}{33}\left(u_y\right)_{17}-\frac{5}{33}\left(u_y\right)_{19}-\frac{1}{528}\left(u_y\right)_{21}+\frac{1}{528}\left(u_y\right)_{25}\right)\\&+o\left(h^6\right)\end{aligned} \tag{91}$$

Acknowledgments

This work was sponsored by the Air Force Office of Scientific Research, USAF, under AFOSR Grants #FA9550-15-1-0268, monitored by Dr. Ivett Leyva. The computations are mainly run on XSEDE resources provided by TACC under grant number TG-ASC090076 supported by National Science Foundation. The views and conclusions contained herein are those of the author and should not be interpreted as necessarily representing the official policies or endorsements either expressed or implied, of the Air Force Office of Scientific Research or the U.S. Government.

References

1. Zhong, X. and X. Wang, *Direct Numerical Simulation on the Receptivity, Instability, and Transition of Hypersonic Boundary Layers.* Annual Review of Fluid Mechanics, Vol 44, 2012. **44**: p. 527-561.
2. Ishihara, T., T. Gotoh, and Y. Kaneda, *Study of High-Reynolds Number Isotropic Turbulence by Direct Numerical Simulation.* Annual Review of Fluid Mechanics, 2009. **41**: p. 165-180.
3. Pirozzoli, S., *Numerical Methods for High-Speed Flows.* Annual Review of Fluid Mechanics, Vol 43, 2011. **43**: p. 163-194.
4. Liu, Y., M. Vinokur, and Z.J. Wang, *Spectral difference method for unstructured grids I: Basic formulation.* Journal of Computational Physics, 2006. **216**(2): p. 780-801.

5. Wang, Z.J., et al., *Spectral difference method for unstructured grids II: Extension to the Euler equations.* Journal of Scientific Computing, 2007. **32**(1): p. 45-71.
6. Wang, Z.J., *Spectral (finite) volume method for conservation laws on unstructured grids - Basic formulation.* Journal of Computational Physics, 2002. **178**(1): p. 210-251.
7. Liu, Y., M. Vinokur, and Z.J. Wang, *Spectral (finite) volume method for conservation laws on unstructured grids V: Extension to three-dimensional systems.* Journal of Computational Physics, 2006. **212**(2): p. 454-472.
8. Patera, A.T., *A SPECTRAL ELEMENT METHOD FOR FLUID-DYNAMICS - LAMINAR-FLOW IN A CHANNEL EXPANSION.* Journal of Computational Physics, 1984. **54**(3): p. 468-488.
9. Dumbser, M., et al., *A unified framework for the construction of one-step finite volume and discontinuous Galerkin schemes on unstructured meshes.* Journal of Computational Physics, 2008. **227**(18): p. 8209-8253.
10. Qiu, J.X., M. Dumbser, and C.W. Shu, *The discontinuous Galerkin method with Lax-Wendroff type time discretizations.* Computer Methods in Applied Mechanics and Engineering, 2005. **194**(42-44): p. 4528-4543.
11. Cockburn, B. and C.W. Shu, *TVB RUNGE-KUTTA LOCAL PROJECTION DISCONTINUOUS GALERKIN FINITE-ELEMENT METHOD FOR CONSERVATION-LAWS .2. GENERAL FRAMEWORK.* Mathematics of Computation, 1989. **52**(186): p. 411-435.
12. Herbert, T. and M.V. Morkovin, *Dialogue on bridging some gaps in stability and transition research.* Laminar-Turbulent Transition. International Union of Theoretical and Applied Mechanics Symposium, 1980: p. 47-72.
13. Morkovin, M.V. and E. Reshotko, *DIALOG ON PROGRESS AND ISSUES IN STABILITY AND TRANSITION RESEARCH.* Laminar-Turbulent Transition, 1990: p. 3-29.
14. Bushnell, D., *Notes on Initial Disturbance Fields for the Transition Problem*, in *Instability and Transition: Materials of the workshop held May 15-June 9, 1989 in Hampton, Virgina*, M.Y. Hussaini and R.G. Voigt, Editors. 1990, Springer US: New York, NY. p. 217-232.
15. Lele, S.K., *Compact Finite-difference Schemes with Spectral-like Resolution.* Journal of Computational Physics, 1992. **103**(1): p. 16-42.
16. Haras, Z. and S. Taasan, *FINITE-DIFFERENCE SCHEMES FOR LONG-TIME INTEGRATION.* Journal of Computational Physics, 1994. **114**(2): p. 265-279.
17. Ashcroft, G. and X. Zhang, *Optimized prefactored compact schemes.* Journal of Computational Physics, 2003. **190**(2): p. 459-477.
18. Hixon, R., *Prefactored small-stencil compact schemes.* Journal of Computational Physics, 2000. **165**(2): p. 522-541.
19. Kim, J.W. and D.J. Lee, *Optimized compact finite difference schemes with maximum resolution.* Aiaa Journal, 1996. **34**(5): p. 887-893.
20. Mahesh, K., *A family of high order finite difference schemes with good spectral resolution.* Journal of Computational Physics, 1998. **145**(1): p. 332-358.
21. Cunha, G. and S. Redonnet, *On the effective accuracy of spectral-like optimized finite-difference schemes for computational aeroacoustics.* Journal of Computational Physics, 2014. **263**: p. 222-232.
22. Zhong, X.L. and M. Tatineni, *High-order non-uniform grid schemes for numerical simulation of hypersonic boundary-layer stability and transition.* Journal of Computational Physics, 2003. **190**(2): p. 419-458.
23. Qiu, J.X. and C.W. Shu, *Hermite WENO schemes and their application as limiters for Runge-Kutta discontinuous Galerkin method: one-dimensional case.* Journal of Computational Physics, 2004. **193**(1): p. 115-135.
24. Qiu, J.X. and C.W. Shu, *Hermite WENO schemes and their application as limiters for Runge-Kutta discontinuous Galerkin method II: Two dimensional case.* Computers & Fluids, 2005. **34**(6): p. 642-663.
25. Zhong, X.L., *High-order finite-difference schemes for numerical simulation of hypersonic boundary-layer transition.* Journal of Computational Physics, 1998. **144**(2): p. 662-709.
26. Hu, S. and X.L. Zhong, *Linear stability of viscous supersonic plane Couette flow.* Physics of Fluids, 1998. **10**(3): p. 709-729.
27. Mundis, N.L., Edoh, A.K., Sankaran, V, "*Highly-Accurate Filter-Based Artificial-Dissipation Schemes for Stiff Unsteady Fluid Systems*," AIAA paper 2016-0072, 2016.
28. Edoh, A.K., Mundis, N.L., Karagozian, A.R., Sankaran, V, "*The Role of Dispersion and Dissipation on Stabilization Strategies for Time-Accurate Simulations*," AIAA paper 2016-0071, 2016